aerospace

MDPI

Article

Numerical Study on Azimuthal Partition Combined Plasma Control for Rotor Airfoil Deep Dynamic Stall at High Advance Ratio

Weihong Kong *, Peng Zhang and Tianxiang Wang

National Key Laboratory of Helicopter Aeromechanics, Nanjing University of Aeronautics and Astronautics, Nanjing 210016, China
* Correspondence: kwhh@nuaa.edu.cn

Abstract

To address the challenge of effectively suppressing deep dynamic stall on the retreating side of rotor blades at high advance ratios, an azimuthal-zone plasma combined control strategy is proposed. This strategy is grounded in the complementary physical mechanisms of AC-DBD and NS-DBD actuators—AC-DBD delays separation onset through continuous momentum injection, while NS-DBD weakens the dynamic stall vortex via pulsed thermal perturbations—and differentially combines the two actuation modes according to the phase-dependent characteristics of dynamic stall evolution at different azimuthal angles on the retreating side, thereby achieving full-cycle, comprehensive dynamic stall suppression. In this study, the unsteady Reynolds-averaged Navier–Stokes (URANS) method, coupled with phenomenological source-term models of AC-DBD and NS-DBD, is employed to numerically investigate the dynamic stall process on the retreating side of rotor blades at high advance ratios. The results demonstrate that the proposed combined control strategy effectively exploits the temporal complementarity of AC-DBD and NS-DBD at different stages of the dynamic stall cycle: during the upstroke phase, AC-DBD provides early intervention through momentum injection; during the stall-development phase, NS-DBD actively modulates the separated shear layer and attenuates the vortex intensity through pulsed actuation; and during the reattachment phase, the two actuators work in synergy to accelerate flow recovery. Quantitative analysis shows that the synergistic control achieves a 13.8% increase in lift and a 20% reduction in lift-coefficient hysteresis-loop area, with control benefits significantly superior to those of single-actuation modes. This study provides a new theoretical basis and technical reference for active flow control of dynamic stall on high-advance-ratio rotors.

Keywords: helicopter; plasma; flow control; dynamic stall; computational fluid dynamics

Check for updates

Academic Editor: Alex Zanotti

Received: 10 August 2026
Revised: 19 September 2026
Accepted: 21 September 2026
Published: 30 September 2026

Copyright: © 2026 by the authors. Licensee MDPI, Basel, Switzerland. This article is an open access article distributed under the terms and conditions of the Creative Commons Attribution (CC BY) license.

1. Introduction

Under high-speed forward flight conditions, the retreating-side blades of a helicopter rotor operate in an unfavorable aerodynamic environment characterized by low local freestream velocity and high angles of attack, which readily induce deep dynamic stall. This phenomenon is accompanied by the generation, convection, and breakdown of large-scale dynamic stall vortices (DSV), leading to a sharp drop in lift, a rapid increase in drag, and severe pitching-moment excursions that critically threaten helicopter handling qualities and flight safety [1]. As the maximum flight speed of helicopters continues to increase, deep

dynamic stall on the retreating side at high advance ratios has become a key bottleneck limiting the expansion of the rotorcraft flight envelope [2].

Greenblatt [2], in a comprehensive review of dynamic stall control, pointed out that retreating blade stall (RBS) in conventional helicopters primarily occurs during high-speed forward flight. As the advance ratio increases, the blade angle-of-attack amplitude exceeds the static stall angle, inducing dynamic stall dominated by the leading-edge vortex (LEV). This results in lift loss, sharp pitching-moment increases, and deterioration of aerodynamic damping, severely limiting the fatigue life of swashplates, bearings, and hub components [2,3]. The pioneering work of McCroskey [3] and Carr et al. [1] established the classification framework for dynamic stall, dividing incompressible dynamic stall into leading-edge stall, trailing-edge stall, and thin-airfoil stall, among which leading-edge stall represents the most challenging type for helicopter applications due to the intense unsteady evolution of the LEV.

To address this challenge, researchers have developed various dynamic stall flow control methods over the past two decades, which can be broadly classified into passive and active approaches [4]. Passive approaches include airfoil geometry optimization and surface-mounted mechanical devices such as vortex generators. Vortex generators delay dynamic stall on thick airfoils by stabilising the flow during the upstroke phase, but this delay is accompanied by an increased maximum lift overshoot and a more severe post-stall lift drop, which can amplify stall-induced vibratory loads [5]. Active approaches require external energy input and include blowing/suction control, synthetic jet control, active twist control, closed-loop control, and plasma flow control. The fundamental time-scale relationship between dynamic stall evolution and periodic forcing was established by Greenblatt and Wygnanski [6], who demonstrated that the effectiveness of unsteady actuation critically depends on the ratio between the excitation frequency and the characteristic frequency of dynamic stall. Han et al. [7] numerically investigated synthetic jet actuation for active dynamic stall control on an OA212 rotor airfoil, demonstrating that synthetic jet actuation effectively reduces the lift hysteresis loop and increases maximum lift, with optimal performance achieved through combined leading-edge (12%c) and trailing-edge (62%c) actuation. Active twist control of helicopter rotor blades has been numerically demonstrated to yield a 10–15% improvement in dynamic-stall-limited forward flight speed and a 5% improvement in stall-limited rotor thrust, at the cost of increased susceptibility to dynamic-stall-induced vibratory loads when the twist actuation is inactive [8]. More recently, closed-loop control strategies have emerged: Nozari and Ebrahimi [9] numerically investigated closed-loop control of dynamic stall on a pitching NACA 0012 airfoil using tandem DBD plasma actuators, demonstrating that feedback-based actuation can outperform open-loop strategies under time-varying flow conditions. Collectively, these studies demonstrate that while a wide spectrum of active control technologies exists, each possesses intrinsic limitations in operating envelope, control authority, or physical mechanism, and no single technique can achieve full-cycle effective control across the entire dynamic stall process. Among these active methods, plasma flow control technology offers distinct advantages such as simple actuator structure, absence of moving parts, light weight, fast response time (microsecond to nanosecond), and wide actuation bandwidth, demonstrating great potential for rotorcraft dynamic stall control applications [4].

Currently, two primary plasma actuation modes are employed for dynamic stall control: alternating-current dielectric barrier discharge (AC-DBD) actuation and nanosecond-pulse dielectric barrier discharge (NS-DBD) actuation. AC-DBD continuously injects momentum into the boundary layer through the "ionic wind" effect, enhancing near-wall flow momentum and thereby delaying separation onset. However, under high-Reynolds-number or deep-stall conditions, its momentum injection is insufficient to overcome the

strong adverse pressure gradient, resulting in significantly diminished control effectiveness [10]. NS-DBD generates localized rapid heating and compression waves (micro-shock waves) through nanosecond pulses, which interact with the separated shear layer to re-energize the flow and promote reattachment. However, NS-DBD is nearly ineffective during the upstroke phase of dynamic stall, because the shear-layer instability has not yet fully developed at this stage, and the pulsed thermal perturbations lack an unstable mode to be amplified [11]. Li et al. [12] conducted unsteady DBD flow control experiments on a rotor airfoil under dynamic stall conditions and found that unsteady actuation can significantly weaken the adverse effects of dynamic stall vortex shedding on airfoil aerodynamics, while generating more small-scale vortices that promote recovery of the leading-edge adverse pressure gradient and flow reattachment. Their results showed that optimal unsteady control performance occurs at actuation frequencies of $F^+ = 1\sim2$, achieving a 16% reduction in lift hysteresis-loop area and a 6% increase in mean lift coefficient. Yu et al. [10] systematically compared the control effectiveness of AC-DBD and NS-DBD for dynamic stall over a NACA0015 airfoil through numerical simulations, finding that the two actuators performed comparably at moderate Reynolds numbers, while NS-DBD significantly outperformed AC-DBD in lift enhancement and hysteresis reduction at high Reynolds numbers, where AC-DBD became nearly ineffective.

The above studies indicate that AC-DBD and NS-DBD possess inherent physical complementarity in dynamic stall control: AC-DBD excels at delaying onset through momentum injection before separation occurs, while NS-DBD excels at weakening the vortex structure and promoting reattachment through thermal perturbations after separation has occurred. However, each single actuation mode has inherent limitations—NS-DBD has almost no control effect during the upstroke phase, while AC-DBD has limited control capability under high-Reynolds-number or deep-stall conditions. Neither can achieve full-cycle effective control throughout the entire dynamic stall process [13]. This limitation stems from the fundamentally different physical mechanisms of the two actuator types: AC-DBD relies on continuous momentum injection, whereas NS-DBD relies on pulsed thermal perturbations. Consequently, each actuator type naturally possesses its own "window of effectiveness" within the dynamic stall cycle—AC-DBD is most effective during the early stage of boundary-layer thickening, while NS-DBD achieves optimal performance only after shear-layer instabilities have fully developed.

In recent years, researchers have begun to explore the synergistic use of AC-DBD and NS-DBD. Takashima et al. [14] experimentally investigated DBD plasma actuators driven by combined sinusoidal AC and nanosecond pulse voltage, finding that the combined-voltage drive enhances the body-force effect of the wall jet, with thrust and power consumption independently controllable via pulse repetition frequency and pulse phase, respectively. Long et al. [15] conducted active flow control experiments on a 20° apex-angle cone-cylinder forebody using both AC and NS plasma actuation, systematically comparing the control effectiveness of the two actuation methods at different freestream velocities in a low-speed wind tunnel. Zhao et al. [16] further performed a numerical study on an airfoil at high angle of attack, comparing the flow control effects of AC-DBD and NS-DBD actuation and analyzing the differences in vorticity transport mechanisms induced by the two actuation modes, demonstrating that the two types of actuation induce spanwise vortices through distinct physical mechanisms—body force for AC-DBD and baroclinic torque for NS-DBD—which provides a physical basis for their synergistic application. These studies demonstrate that coordinated or combined use of AC-DBD and NS-DBD actuators is technically feasible.These studies demonstrate that coordinated or combined use of AC-DBD and NS-DBD actuators is technically feasible.

Meanwhile, researchers have begun to investigate the azimuthal effect of plasma flow control on rotors in forward flight. Studies have shown [17] that the flow field around forward-flight rotor blades is significantly influenced by azimuthal angle, exhibiting strong spatiotemporal non-uniformity; a complete flow evolution cycle can be divided into initial separation, flow reattachment, and secondary separation phases. The separation patterns, vortex-structure evolution, and control requirements on the blade surface differ fundamentally across azimuthal angles—different azimuthal angles on the retreating side correspond to different dynamic stall phases, and thus require different actuation types, timings, and control intensities. This provides a physical basis for azimuthal-zone-based differentiated plasma control strategies.

In summary, existing plasma-based dynamic stall control studies still suffer from the following deficiencies. First, most studies employ a single actuation mode (either AC-DBD or NS-DBD) and fail to exploit the temporal complementarity of the two actuator types at different phases of the dynamic stall cycle to achieve phase-differentiated control. Second, existing studies are mostly based on two-dimensional airfoil pitching-oscillation conditions, while research on control strategies specifically designed for the spatiotemporal azimuthal variations in actual rotor forward flight remains rather limited [4]. Although the individual control effectiveness of AC-DBD and NS-DBD has been extensively validated, the synergistic enhancement mechanism of their combined use and its applicability to azimuthal-zone control of rotors have not yet been systematically investigated.

To address the above issues, this paper proposes an azimuthal-zone plasma combined control strategy for deep dynamic stall on high-advance-ratio rotors. The core concept of this strategy is: based on the phase-dependent characteristics of dynamic stall evolution at different azimuthal angles on the retreating side, the retreating side is divided into several control zones, within which AC-DBD and NS-DBD are differentially combined—during the upstroke phase, AC-DBD provides continuous momentum injection to delay separation onset; during the stall-development phase, NS-DBD provides pulsed thermal perturbations to weaken the dynamic stall vortex intensity; and during the reattachment phase, the two actuators work in synergy to accelerate flow recovery—thereby achieving full-cycle, comprehensive dynamic stall suppression. In this study, the unsteady Reynolds-averaged Navier–Stokes (URANS) method, coupled with phenomenological source-term models of AC-DBD and NS-DBD, is employed to numerically investigate the dynamic stall process on the retreating side of high-advance-ratio rotors [18]. The synergistic enhancement mechanisms and parametric influences of the combined control strategy are systematically analyzed, aiming to provide a new theoretical basis and technical reference for active flow control of dynamic stall on high-advance-ratio rotors.

2. Methods

2.1. Numerical Methods and Mathematical Models

2.1.1. Computational Model

Within the numerical simulation framework of computational fluid dynamics (CFD), fluid dynamic behavior is governed by a set of mathematical equations representing the fundamental physical conservation laws. Strictly adhering to the conservation laws of mass, momentum, and energy, these equations are collectively referred to as the Navier–Stokes (N-S) equations and can be formulated in either differential or integral form depending on the specific requirements of the numerical solution. For nanosecond-pulse dielectric barrier discharge (NS-DBD) actuation, given that previous studies have demonstrated the extremely low macroscopic flow velocity induced thereby, the momentum injection effect (i.e., body force) is typically regarded as a secondary factor and thus neglected. Based on this assumption, the body force source term is set to zero in the present study, and the

unsteady compressible Navier–Stokes equations coupled with an energy source term are formulated in an inertial reference frame, expressed as follows:

$$\frac{\partial \rho}{\partial t} + \frac{\partial (\rho u_i)}{\partial x_i} = 0 \tag{1}$$

$$\frac{\partial (\rho u_i)}{\partial t} + \frac{\partial (\rho u_i u_j)}{\partial x_j} = -\frac{\partial p}{\partial x_i} + \frac{\partial \tau_{ij}}{\partial x_j} \tag{2}$$

$$\frac{\partial (\rho E)}{\partial t} + \frac{\partial [u_i(\rho E + p)]}{\partial x_i} = \frac{\partial (\tau_{ij} u_j)}{\partial x_i} + \frac{\partial \left(\frac{\lambda \partial T}{\partial x_i} \right)}{\partial x_i} + Q \tag{3}$$

$$\tau_{ij} = \mu \left(\frac{\partial u_i}{\partial x_j} + \frac{\partial u_j}{\partial x_i} \right) - \frac{2}{3} \mu \frac{\partial u_k}{\partial x_k} \delta_{ij} \tag{4}$$

Equation (1) represents the mass conservation equation, and Equation (2) denotes the momentum conservation equation. Equation (3) is the energy conservation equation augmented with an energy source term, while Equation (4) provides the supplementary constitutive relation for the viscous stress tensor in terms of the strain rate. In the above equations, ρ denotes the fluid density, p the fluid pressure, μ the dynamic viscosity, τ_{ij} the viscous stress tensor, and the δ_{ij} Kronecker delta. The variables u_i and u_j represent the x and y components of the velocity vector, respectively; T is the fluid temperature; and Q denotes the power density of gas heating during the NS plasma discharge. The gas is assumed to be an ideal gas. The thermal conductivity is determined by an empirical correlation, and the dynamic viscosity is related to the temperature via Sutherland's law:

$$\mu = \frac{A_s T^{3/2}}{T + T_s} \tag{5}$$

where T_s = 110.4 K denotes the Sutherland temperature, $A_s = \mu_\infty (T_\infty + T_s)/{T_\infty}^{3/2}$ denotes the Sutherland constant, T_∞ the freestream temperature, and μ_∞ the freestream dynamic viscosity.

In this study investigating the effects of nanosecond-pulse plasma actuation on the aerodynamic characteristics of rotor airfoils, the plasma actuator is deployed on the upper surface of the airfoil leading edge, with the actuation region situated in the near-wall region. The directed energy input induced by this actuation gives rise to significant turbulence anisotropy. By directly solving the transport equations of the Reynolds stress tensor, the Reynolds stress model (RSM) can accurately capture such anisotropic features. Furthermore, the Reynolds stress transport equations in the RSM inherently incorporate transient and source terms, enabling the precise capture of the temporal evolution characteristics of turbulent stresses under non-equilibrium conditions (where the time scale of the nanosecond pulse is on the order of nanoseconds, whereas the turbulent characteristic time is typically on the order of microseconds). Consequently, the RSM turbulence model is employed in the present study. For the nanosecond-pulse plasma flow incorporating an energy source term, its general form can be expressed as follows:

$$\frac{\partial \overline{u_i' u_j'}}{\partial t} + \overline{u_k} \frac{\partial \overline{u_i' u_j'}}{\partial x_k} = D_{ij} + P_{ij} + \Phi_{ij} - \varepsilon_{ij} + S_{ij} \tag{6}$$

$$\frac{\partial \varepsilon}{\partial t} + \overline{u_k} \frac{\partial \varepsilon}{\partial x_k} = C_{\varepsilon 1} \frac{\varepsilon}{k} P_k - C_{\varepsilon 2} \frac{\varepsilon^2}{k} + \frac{\partial}{\partial x_k} \left(\left(\nu + \frac{\nu_t}{\sigma_\varepsilon} \right) \frac{\partial \varepsilon}{\partial x_k} \right) + S_\varepsilon \tag{7}$$

$$D_{ij} = \frac{\partial}{\partial x_k} \left(\nu_t \frac{\partial \overline{u_{i'} u_{j'}}}{\partial x_k} + C_s \frac{k}{\varepsilon} \overline{u_{k'} u_{l'}} \frac{\partial \overline{u_{i'} u_{j'}}}{\partial x_l} \right) \tag{8}$$

$$P_{ij} = -\left(\overline{u_{i'}u_{k'}}\frac{\partial \overline{u_j}}{\partial x_k} + \overline{u_{j'}u_{k'}}\frac{\partial \overline{u_i}}{\partial x_k}\right) \tag{9}$$

The numerical computations in this study are based on the governing equations for incompressible flow. Considering the requirements for accuracy and efficiency in computing the two-dimensional airfoil flow field, the finite volume method, which is well-established in engineering applications and offers the advantages of both computational stability and conservation, is employed for the discrete solution of the governing equations. For the pressure-velocity coupling, the SIMPLEC algorithm is adopted. Compared to the SIMPLE algorithm, the SIMPLEC algorithm optimizes the pressure correction equation, thereby enhancing numerical stability and convergence efficiency, while adhering to the core logic of the pressure correction method by achieving coupling through the segregated solution of the continuity and momentum equations. To provide more reliable data for analyzing flow characteristics, a third-order density scheme is employed to more accurately capture the density distribution and its variations in the flow field. The boundary conditions are configured as follows: a velocity inlet is applied at the inlet of the computational domain, and a pressure outlet at the outlet. The airfoil surface is set as a no-slip adiabatic wall to accurately reflect the interaction characteristics between the airfoil surface and the fluid in the actual flow field. The specific parameter configuration for the plasma actuation region and the coupling treatment of the energy source term will be elaborated in detail in the subsequent sections.

2.1.2. Computational Domain

As one of the core components of computational fluid dynamics (CFD) methodologies, mesh generation provides the computational cells and nodes for the numerical simulations. The mesh quality directly affects the stability and convergence rate of the numerical calculations; therefore, generating a high-quality mesh is a prerequisite for ensuring the accuracy of the CFD results. Grids are predominantly classified into structured and unstructured types. In this study, a structured mesh is employed due to its advantage in facilitating high-order numerical schemes. The selected airfoil is the NACA0015, with local mesh refinement applied in the dielectric barrier discharge (DBD) plasma actuation region. High-quality body-fitted meshes around the airfoil play a crucial role and serve as the foundation for high-fidelity numerical simulations. It is worth noting that the Reynolds Stress Model (RSM) employed in this study imposes strict requirements on the near-wall mesh resolution, making the refinement of the boundary layer an indispensable step. The determination of the first-layer height for the boundary layer is based on the following formula:

$$y = \frac{y^+ \mu}{U_\tau \rho} \tag{10}$$

$$U_\tau = \sqrt{\frac{\tau_w}{\rho}} \tag{11}$$

$$\tau_w = 0.029 \mathrm{Re}^{-0.2} \rho u_\infty^2 \tag{12}$$

$$\mathrm{Re} = \frac{\rho U_\infty c}{\mu} \tag{13}$$

where μ is the dynamic viscosity, Re is the Reynolds number, U_∞ is the freestream velocity, c is the chord length, U_τ is the estimated velocity of the near-wall shear flow, τ_w is the wall shear stress, and ρ is the air density. According to the near-wall mesh requirements of the RSM turbulence model, the dimensionless wall distance is set to $y^+ = 1$, and the mesh growth rate is typically selected within the range of 1.1 to 1.3; in this study, it is set to 1.2.

The computational domain and mesh are illustrated in Figure 1. The domain is divided into an inner zone and an outer zone, with a total of 150,000 cells. The outer zone is a rectangular region with a length of 25 chord lengths and a width of 20 chord lengths, discretized using unstructured mesh. The inner zone is a circular region with a radius of 3 chord lengths, discretized using structured mesh, with its center located at the quarter-chord position of the airfoil. The first cell height is set to 10^{-5} m, the cell growth ratio from the wall outward is 1.1, and 10 layers are arranged in the boundary layer. The sliding mesh technique is employed: the inner zone mesh undergoes rigid body motion together with the airfoil, while the outer zone mesh remains stationary, thereby avoiding mesh deformation induced by the airfoil motion.

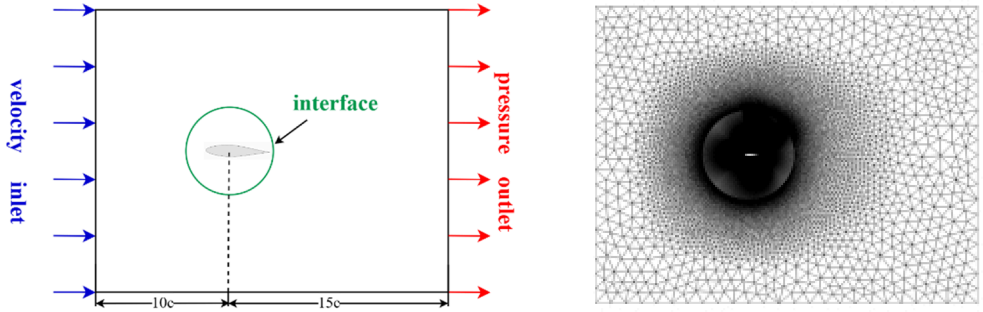


Figure 1. Computational domain and mesh.

2.1.3. Mathematical Model of Nanosecond Pulse Dielectric Barrier Discharge Plasma

For the phenomenological modeling of the nanosecond-pulse dielectric barrier discharge (NS-DBD) plasma, the present study neglects the edge effects of the actuator and assumes a uniform spanwise discharge along the electrodes, thereby simplifying the NS-DBD actuation into a two-dimensional model to reduce computational complexity. The development of this model centers on four key elements: the single-discharge energy per unit span of the actuator, the fraction of the discharge energy utilized for gas heating, the spatial density distribution and effective region of the energy deposition, and the timescale of energy deposition. Among these, the single-pulse discharge energy serves as the core parameter characterizing the actuation intensity κ and directly governing the flow control effectiveness; its value can be derived from the voltage–current waveforms of the NS-DBD. Theoretically, the discharge energy is influenced by multiple factors, including the rising edge of the voltage signal, peak voltage, voltage polarity, and ambient pressure. In accordance with the specific operating conditions of this study, only three key influencing factors—peak voltage, ambient pressure, and pulse frequency—are primarily considered here [19].

Takashima et al. [20] experimentally investigated the correlation between the discharge energy of the NS-DBD and its discharge parameters. At an actuation pulse frequency of 10 Hz, the functional relationship between the single-pulse discharge energy $E_{10}^{\mathrm{Energy}(U)}$ and the peak actuation voltage U is given by:

$$E_{10}^{\mathrm{Energy}(U)} = 0.0008365 \times U^{2.476} \tag{14}$$

Furthermore, the experiments also demonstrated that the single-pulse discharge energy is influenced by the discharge pulse frequency (Hz). With all other parameters held constant, a higher frequency yields a greater single-pulse energy input. Under atmospheric pressure conditions (760 torr, 1 *torr* $\approx$ 1.33 $\times$ 102 Pa), the expression for the single

nanosecond-pulse energy input per unit span of the actuator as a function of voltage and frequency is given as follows:

$$E_{\text{Energy}}(f, U) = \frac{a \times f^b + c}{a \times 10^b + c} \times E^{10}_{\text{Energy}}(U) \tag{15}$$

Considering that variations in ambient pressure alter the gas density and discharge characteristics, the discharge energy is assumed to be approximately linearly dependent on the ambient pressure. By incorporating the relationship between the single-pulse discharge energy and the applied voltage, the experimental data U = 12 kV obtained under the specified conditions and within a pressure range of 200–1400 torr are fitted to yield: $Eenergy(p) = -0.001781p + 9.924$, where the p expressed in torr. Subsequently, by combining this with the relationship between the peak voltage and the discharge energy, the following expression is derived:

$$E_{\text{Energy}}(p, U) = \frac{E_{\text{Energy}}(U)}{E_{\text{Energy}}(12)} \times (-0.001781p + 9.924) \tag{16}$$

Ultimately, the single-discharge energy of the actuator in operation, accounting for the three factors of actuation voltage, pulse frequency, and ambient pressure, is obtained as follows $Energy(f, U, p)$, with the unit of mJ/cm,

$$E_{\text{Energy}}(f, U, p) = \frac{mp + n}{760m + n} \times \frac{a \times f^b + c}{a \times 10^b + c} \times E^{10}_{\text{Energy}} \tag{17}$$

where the coefficients are a = 0.2772, b = 0.4585, c = 7.991, m = −0.001781, n = 9.924; Secondly, the fraction of discharge energy utilized for gas heating is primarily influenced by the reduced electric field strength E/N, with the unit expressed in Townsend (Td), where Td (1 Td = 10−17 V·cm^2). The electric field strength E depends on the actuation voltage and the geometric configuration of the actuator; in engineering applications, it is commonly approximated as $E = U/D$, while the gas number density N is related to the ambient pressure and temperature. By fitting the curve of the heating efficiency η as a function of the reduced electric field strength (ranging from 100 to 1000 Td) under dry air conditions reported in Ref. [19], the following expression is obtained:

$$\eta = 0.01107 \times (E/N)^{0.5534}, \quad (100 < E/N < 1000) \tag{18}$$

Assuming that the energy used for gas heating is proportional to the radiation intensity, the spatial distribution function of the radiation intensity can be derived from the radiation intensity data, thereby yielding the spatial distribution function of the gas heating energy. Let the radiation intensity at a point within the plasma region be denoted as $Emission(x,y)$.

$$\text{Emission}(x, y) = \frac{F(x)}{\frac{1}{L}\int_0^L F(x)\mathrm{d}x} \times \frac{G(y)}{\frac{1}{H}\int_0^H G(y)\mathrm{d}y} \tag{19}$$

$F(x)$, $G(y)$ which represents the fit to the curves of radiation intensity variation along the x and y directions shown in the figure above. Consequently, the total radiation intensity within the plasma region is given by

$$\text{Emission}_{\text{total}} = \int_0^L \int_0^H \text{Emission}(x, y)dxdy \tag{20}$$

By analyzing the voltage–current waveforms of typical nanosecond-pulse plasma aerodynamic actuators and calculating the temporal evolution of power, it is observed that

the power exhibits a characteristic triangular pulse distribution over time. Consistent with the core assumption of the phenomenological model—that the temporal variation in the heat source aligns with the power evolution—the temporal distribution of the heat source in this study is simplified as a symmetric triangular pulse with a peak value of 1 and equal rise and fall times, where the pulse duration is explicitly defined as being equivalent to the actuation pulse width [19]. The temporal distribution function is expressed as $S(t)$:

$$S(t) = \begin{cases} t/25 & 0\ \text{ns} \leqslant t \leqslant 25\ \text{ns} \\ 2 - t/25 & 25\ \text{ns} < t \leqslant 50\ \text{ns} \\ 0 & t > 50\ \text{ns} \end{cases} \tag{21}$$

Based on the aforementioned assumptions, the spatial distribution function of the energy can be expressed as

$$\text{Power}_{\text{th}}(x, y) = \frac{\text{Emission}(x, y)}{\text{Emission}_{\text{total}}} \times \frac{E_{\text{energy}}(p, f, U) \times \eta}{\Delta t} \times S(t) \tag{22}$$

This is coupled as a source term into the energy equation of the governing Equation (3).

2.1.4. Mathematical Model of Alternating Current Dielectric Barrier Discharge Plasma

In the simulation and modeling of AC dielectric barrier discharge (AC-DBD) plasma, based on experimental measurements and curve fitting, Shyy [21] further proposed an empirical expression for the spatial distribution of the body force, approximating the force field within the actuation region as a triangular vector distribution, where the direction and magnitude of the body force vary spatially and are parameterized by empirical formulas, thereby preserving the primary features of AC-DBD induced boundary layer acceleration and separation modulation at a reduced computational cost:

$$\left|\overline{E}\right| = E_0 - k_1 x - k_2 y \tag{23}$$

$$E_x = \frac{|E| k_2}{\sqrt{k_1^2 + k_2^2}}, E_y = \frac{|E| k_1}{\sqrt{k_1^2 + k_2^2}} \tag{24}$$

The parameters in the above equation $E_0 = 2.26 \times 10^7$ V/m, k_1, k_2 are the gradient constants for the electric field distribution along the x and y directions, with values of $k_1 = 6.54 \times 10^9$ V/m^2, $k_2 = 1.31 \times 10^{10}$ V/m^2. The distribution of the body force generated by momentum transfer from collisions between charged particles and neutral air molecules under the action of the electric field is expressed as follows:

$$\begin{aligned} F_{tave,x} &= \vartheta \alpha \delta \rho_c e_c \Delta t E_x \\ F_{tave,y} &= \vartheta \alpha \delta \rho_c e_c \Delta t E_y \end{aligned} \tag{25}$$

The values of the parameters in the above equation are $\alpha = 1$, $\vartheta = 3$ kHz, $e_c = 1.6 \times 10^{-19}$ C, $\Delta t = 67$ μs, $\rho_c = 1 \times 10^{17}$/m^3, where δ is the body force correction parameter, whose value is determined by the electric field intensity in the discharge region:

$$\begin{cases} \delta = 0, |E| < E_{cr} \\ \delta = 1, |E| > E_{cr} \end{cases} \tag{26}$$

where E_{cr} is the breakdown electric field strength, with a value of $E_{cr} = 3 \times 10^6$ V/m^2. When the electric field intensity in the discharge region is lower than the breakdown electric field strength, the air cannot be ionized to generate plasma; in this case, the value of δ is

set to 0, otherwise it is taken as 1. The aforementioned body force generated by plasma actuation is incorporated as a source term into the solution of the Navier–Stokes equations. The expression for the body force source term is shown in Equation (20), where represents the magnitude parameter of the body force vector generated by dielectric barrier discharge plasma actuation, which characterizes the intensity of ℜ the plasma discharge.

$$F_i = \begin{bmatrix} 0 \\ F_{x,\text{plasam}} \\ F_{y,plasma} \end{bmatrix} = \begin{bmatrix} 0 \\ \Re\alpha\vartheta\rho_c e_c \Delta t E'_x \\ \Re\alpha\vartheta\rho_c e_c \Delta t E'_y \end{bmatrix} \quad (27)$$

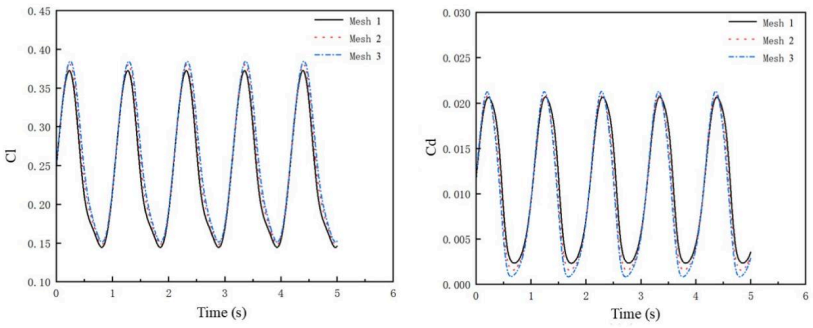
In this study, the actuation effect of alternating current dielectric barrier discharge (AC-DBD) plasma is incorporated into the Fluent solver as a source term. Considering that the heat generated during the AC-DBD plasma discharge process is limited and the resulting temperature rise has a negligible disturbance on the flow field, this study focuses solely on its acceleration effect on the airflow. Consequently, the discharge actuation process is equivalent to a momentum source term, which is introduced into the governing equations for solution.

2.2. Numerical Simulation Validation

2.2.1. Grid Independence Verification

For the NACA0015 airfoil case undergoing pitching motion, three computational meshes with different levels of refinement (Mesh1, Mesh2, and Mesh3) were constructed for comparative validation. The number of grid cells in these meshes are 149,844, 199,792, and 249,740, respectively. The lift coefficient *Cl* and drag coefficient *Cd* of the airfoil were selected as the primary indicators for the grid independence assessment. During the grid independence verification, the pitching parameters for the NACA0015 airfoil were set as follows: free-stream velocity U_∞ = 20 m/s, reduced frequency k = 0.03, mean angle of attack $a_0 = 8°$, and pitching amplitude $a_1 = 7°$. The variation in the angle of attack during the pitching motion follows the equation: $\alpha = a_0 + a_1 \sin(2*k*U_\infty/c*t)$, where the definition of the reduced frequency is given by $k = wc/U_\infty$. The computational time step was set to 0.01 s, with a total simulation time of 5 s, resulting in 500 output steps. Over this duration, the airfoil completed five full pitching cycles.

Figure 2a,b present the comparison of the time histories of the lift coefficient (*Cl*) and drag coefficient (*Cd*) for the three different meshes (Mesh 1, Mesh 2, and Mesh 3). As shown in the figures, the aerodynamic force curves for all three meshes exhibit periodic characteristics, and their overall trends are highly consistent, indicating that mesh refinement has a minor impact on the unsteady aerodynamic response of the airfoil under this operating condition. Regarding the lift coefficient, the peak and trough positions of the curves obtained from the three meshes basically coincide.



(a) **Time history of lift coefficient (Cl)** (b) **Time history of drag coefficient (Cd)**

Figure 2. Grid independence verification.

2.2.2. Validation Case for the Pitching Motion of the NACA0015 Airfoil

In this validation case, the NACA0015 airfoil is selected as the research object, with a chord length set to c = 0.2023 m. The free-stream velocity is set to U_∞ = 20 m/s, corresponding to a Reynolds number of $Re = 2.5 \times 10^5$ based on the chord length. The airfoil undergoes periodic pitching motion about the quarter-chord point, with a reduced frequency of k = 0.05. These operating parameters are referenced from the experimental studies by Singhal et al. [22]. The computed aerodynamic parameters of the airfoil show good agreement with the experimental data in terms of both magnitude and trend, as illustrated in Figure 3. This confirms the reliability of the numerical method employed in this study for simulating pitching airfoils.

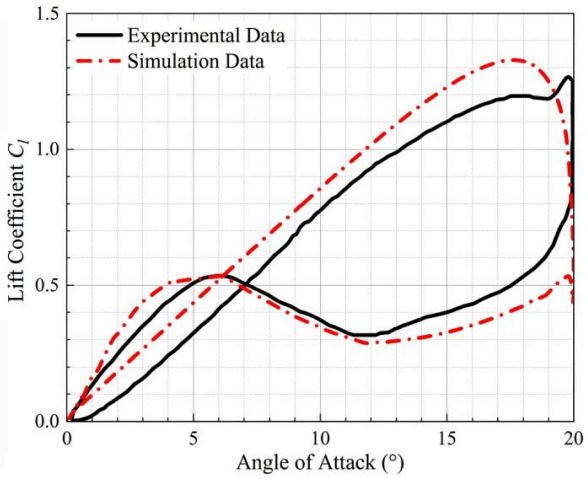


Figure 3. Comparison between numerical results and experimental values for NACA 0015 airfoil pitchin.

Figure 4 shows the variation in lift coefficient with angle of attack at four time step sizes: t = 0.0200, 0.0050, 0.0025, and 0.0010 s. As can be seen from the figure, the curve obtained with Δt = 0.0200 s shifts downward significantly compared with the other three time step sizes, whereas the curves corresponding tot = 0.0050, 0.0025, and 0.0010 s show good agreement with each other. This demonstrates that the computational results become independent of the time step size when t ≤ 0.005 s. To further improve computational accuracy, the smallest time step size is adopted in this study, and therefore t = 0.0010 s is selected for all subsequent calculations.

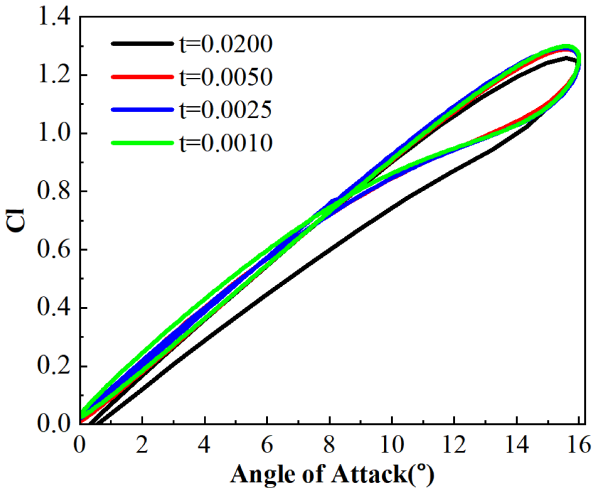


Figure 4. Time-step independence study.

2.2.3. Numerical Simulation Validation of Nanosecond Dielectric Barrier Discharge Plasma

In this section, a two-dimensional flat plate case is employed to validate the nanosecond pulse dielectric barrier discharge (NS-DBD) plasma mathematical model established earlier. The model parameters are set based on the actuator configuration and experimental results reported in Reference [23] (pulse width of 50 ns, voltage of 50 kV). The plasma effect is coupled within a rectangular region of the flow field, which simulates the effective ionization zone formed between the buried electrode and the exposed electrode, roughly following the effective electric field range generated by the plasma discharge. The length of this rectangular plasma region is l_1 = 6 mm, and its height is l_2 = 0.6 mm. The plasma actuator is mounted on the bottom flat plate; therefore, the bottom surface of the 2D flat plate is defined as a no-slip adiabatic wall. To intuitively observe the disturbance characteristics of the plasma on a quiescent flow field and to match the experimental conditions, the initial flow velocity is set to U_∞ = 0 m/s.

The numerical simulation employs a laminar model combined with an unsteady calculation method. The discharge process of nanosecond plasma is a typical transient problem involving strong disturbances. To ensure the accuracy of simulating the pulse loading and heating processes, the time step is set to 1 ns during the pulse loading phase. After the pulse loading ends, a variable time-step strategy is adopted to gradually increase the time step, thereby balancing computational accuracy and efficiency. Furthermore, the number of iterations per time step is set to 40. Through residual monitoring and iteration convergence analysis, the convergence of the numerical calculation and the conservation of physical quantities are ensured. The initial conditions of the flow field are set as follows: the temperature is constant at 26.85 °C; the gas is treated as an ideal gas with a density of $\rho = 1.223 \times 10^3$ kg/m^3; the viscosity is calculated using the Sutherland model. Since the flow remains laminar from the inlet to the outlet along the bottom wall, the core objective of this validation is to compare the wave speed and intensity of the induced shock wave between the numerical simulation and the experiment. This comparison serves as the key basis for determining whether the mathematical model can accurately characterize the disturbance properties of nanosecond plasma.

Figure 5 presents a comparison between the experimental schlieren [24] and tnumerical schlieren results. The top row displays the experimental schlieren images, while the bottom row shows the numerical schlieren results obtained based on the mathematical model proposed in this study. As clearly observed from the figures, after applying the nanosecond dielectric barrier plasma actuation, two arc-shaped shock wave structures of different sizes are generated ahead of and behind the plasma region. At the initial moment, the shock waves exhibit a distinct double-arc morphology, propagating outward from the plasma region. As time progresses, the two shock waves continue to expand outward and gradually interact with each other. By 16 μs, the shock waves have moved further outward, and their intensity has gradually attenuated. In terms of the development process of the shock wave motion, the numerical simulation results show good agreement with the experimental results regarding the morphological evolution, propagation speed, and intensity attenuation laws of the shock waves.

Since the discharge process of nanosecond pulse plasma lasts only tens of nanoseconds and is accompanied by electromagnetic interference, it is difficult to obtain detailed experimental data. To further quantitatively analyze the accuracy of the plasma mathematical model, a vertical monitoring line is set within the plasma region to extract the pressure distribution characteristics of the shock wave at different time instants, and these results are compared quantitatively with the simulation data from the literature.

Figure 6 shows the comparison between the overpressure profiles obtained from the numerical simulation at different time instants and the data from Reference [24]. These

results demonstrate that the plasma numerical model established in this study can accurately characterize the generation, propagation, and attenuation processes of the shock wave pressure. The predicted shock wave pressures fall within a reasonable physical range, thereby effectively validating the reliability of the model.

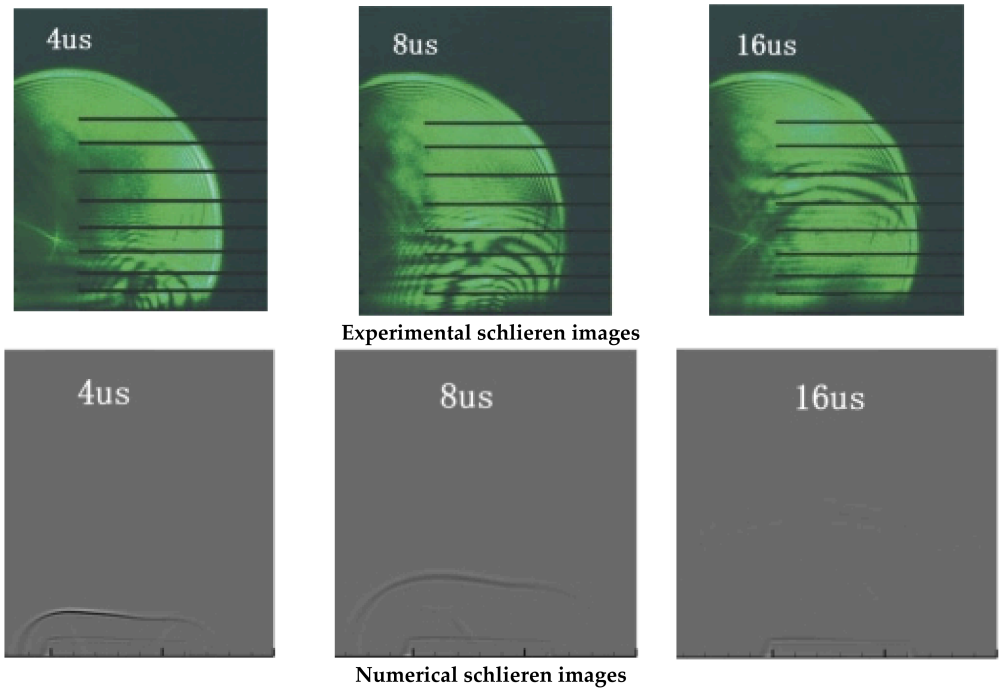


Figure 5. Comparison of experimental and numerical schlieren images.

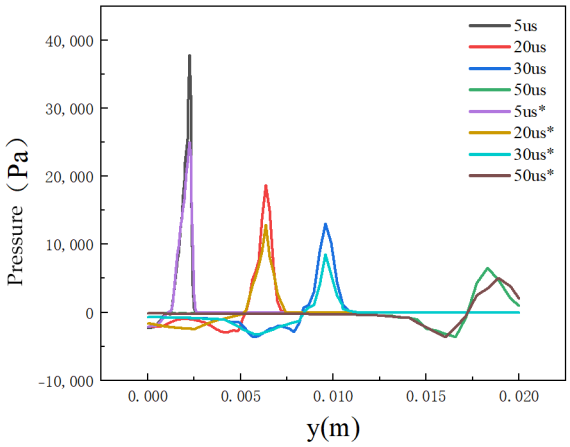


Figure 6. Comparison of overpressure profiles at different times with data from literature. * represents reference data.

2.2.4. Numerical Simulation of Alternating Current Dielectric Barrier Discharge Plasma

The model parameters are established based on the Shyy model, which is currently the most widely used model in AC-DBD plasma numerical simulations. The units for E_0, k_1, k_2, α, δ, ρ_c, Ecr, and *Ecr* have been specified. These parameters are configured to simulate the plasma intensity corresponding to a peak voltage of V_{max} = 12 kV in the experiment. The left end of the flat plate serves as the flow inlet, located 10 cm from the right side of the plasma actuator region, while the right end serves as the flow outlet, located 10 cm from the left side of the plasma actuator region. The height of the entire validation domain is 12 cm. The temperature is set to a constant 20 °C, the gas density is set to $\rho = 1.223 \times 10^3$ kg/m^3,

and the gas viscosity is set to $\mu = 1.7895 \times 10^{-5}$. The computational domain of the flat plate is shown in Figure 7.

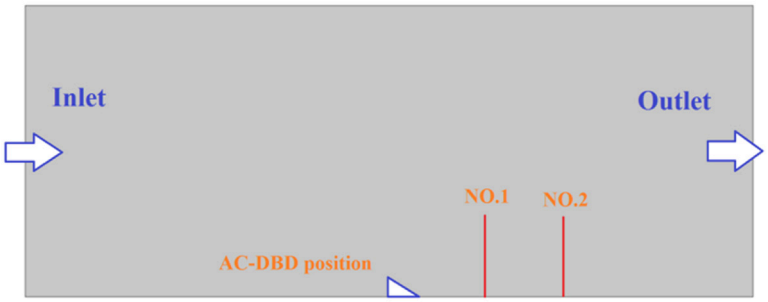


Figure 7. Schematic of flat plate validation.

In the validation, two velocity measurement lines are placed at downstream distances of 1 cm and 2 cm from the plasma actuator location to capture the velocity variations downstream after plasma discharge. These correspond to Measurement Location 1 and Measurement Location 2, respectively. During the AC-DBD flat plate validation process, the initial flow velocity is set to 0 m/s. Setting the flow velocity to zero allows for a clearer observation of the disturbance induced by the plasma on the flow field, thereby distinctly demonstrating the plasma control effect.

In Figure 8, the results indicate that the maximum velocity at Measurement Location 1 occurs at a height of 0.1 cm above the surface, reaching approximately 5.4 m/s, while the maximum velocity at Measurement Location 2 occurs at a height of 0.2 cm, reaching approximately 3.8 m/s. A comparison with the experimental data from Reference [20] shows that the experimentally induced jet peak velocity is 5.2 m/s, and the experimental values at the two data collection points range between 3.8 m/s and 5.4 m/s. Therefore, it can be concluded that the model achieves accurate precision.

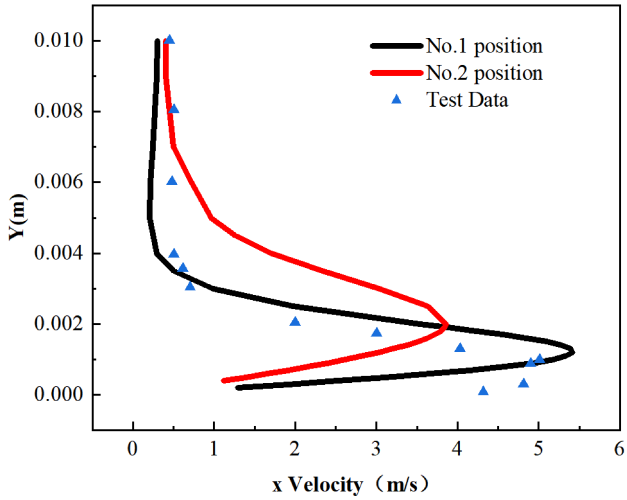


Figure 8. Comparison of induced velocity at measurement points with experimental data.

3. Results

3.1. Control Mechanisms of Different Plasma Actuation Modes

To deeply reveal the essential nature of flow control by different types of dielectric barrier discharge (DBD) plasmas, this section focuses on the NACA0015 airfoil. Two actuation forms, alternating current DBD (AC-DBD) and nanosecond pulse DBD (NS-DBD), are employed. Under the premise of keeping the airfoil geometric parameters, incoming

flow conditions, and other settings completely consistent, the actuation effects of both methods under various operating conditions are systematically compared, and the essential differences in their control mechanisms are analyzed.

As intuitively shown in the flow field contours of Figure 9, regardless of whether the free-stream velocity is at Ma = 0.1 or Ma = 0.3, significant large-scale separation vortices exist downstream of the airfoil when the actuation is off. The streamlines exhibit large-scale closed loops in the rear part of the airfoil, indicating severe flow separation, with the separation zone occupying a substantial area near the trailing edge. When AC-DBD actuation is activated, the scale of separation vortices on the airfoil surface significantly decreases at Ma = 0.1, and the closed streamline region contracts markedly, leaving only a small range of separation at the tail. However, when the free-stream velocity increases to Ma = 0.3, the scale of separation vortices on the airfoil surface remains basically unchanged. This phenomenon occurs because AC-DBD enhances momentum transport within the boundary layer through continuous body force injection, thereby suppressing the development of separation. As the free-stream velocity increases, the proportion of momentum added by AC-DBD relative to the free-stream momentum gradually decreases, leading to a deterioration in its actuation effectiveness. In contrast, when NS-DBD actuation is activated at Ma = 0.3, the airfoil flow field exhibits characteristics completely different from those of AC-DBD: discrete vortex structures are generated in the flow field. These vortices mix with the mainstream flow downstream of the airfoil, directly disrupting the original large-scale separation vortices. Unlike AC-DBD, which primarily functions by suppressing the size of separation vortices, NS-DBD achieves active reconstruction of the separation zone by actively inducing vortex structures, transforming the separation morphology from continuous large vortices into discrete small vortices. It is worth noting that at lower free-stream velocities, the energy exchange between the induced vortices and the mainstream weakens, causing the energy of the vortex structures to dissipate rapidly, thereby reducing their actuation effectiveness.

3.2. Static Aerodynamic Characteristics Under NS-DBD Actuation

3.2.1. Effect of Actuator Installation Position

This section investigates the effects of nanosecond pulse plasma actuation installed at different leading-edge positions on the aerodynamic characteristics of the NACA0015 airfoil. The plasma actuators are positioned along the chordwise direction at 1.51%c, 3.15%c, 6.18%c, and 9.18%c. The schematic diagram of the plasma actuators installed at different leading-edge positions is shown in Figure 10.

By comparing and analyzing the differences in flow field structures under the conditions of Ma = 0.1 and Ma = 0.3, the comparison of calculation results is as follows:

From the comparison of plasma actuation effects at different installation positions shown in Figure 11, it can be observed that when the actuator is installed near the leading edge at 1.51%c, multiple small-scale discrete vortices are induced under the Ma = 0.1 condition. These vortices are generated sequentially along the upper surface of the airfoil and transported downstream. Under the Ma = 0.3 condition, the generation and transport of these small vortices remain basically consistent, and the separation zone is divided into multiple vortex core regions. However, due to the proximity to the leading edge, the vortices induced by the actuation do not effectively reduce the separation zone, and the resulting protrusions increase drag to some extent.

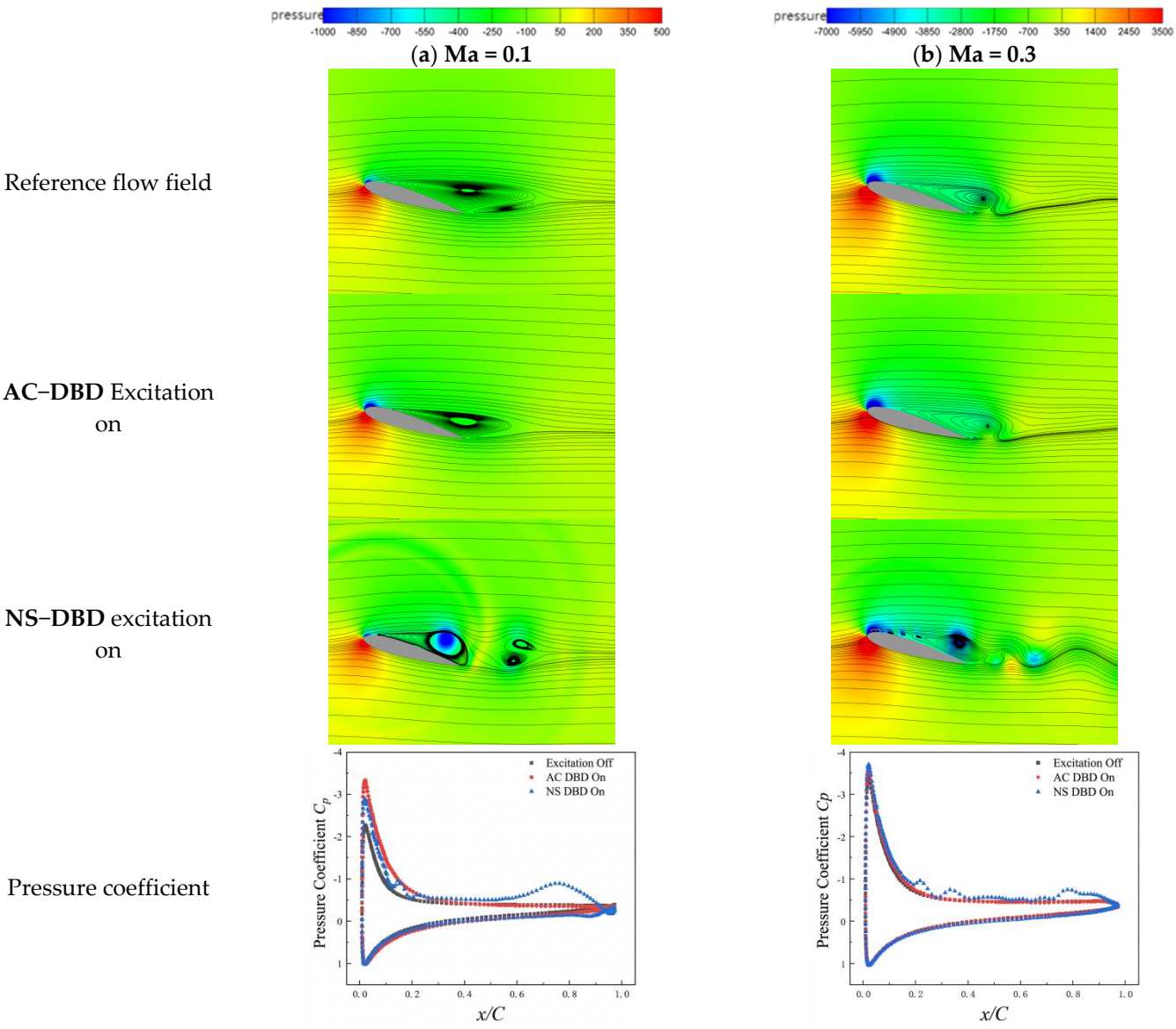


Figure 9. Comparison of flow field lines at different velocities and comparison of pressure coefficients.



Figure 10. Schematic of different installation locations of plasma actuators at the airfoil leading edge.

The actuator installed at 3.15%c is located precisely within the region of strong adverse pressure gradient near the leading edge at high angles of attack, which is also the sensitive location where laminar separation bubbles originate. The localized body force generated by the actuator at this position most effectively excites the shear layer instability, inducing the formation of small, controlled reattachment vortices near the wall. This "source intervention" mechanism significantly enhances momentum mixing between the mainstream and the boundary layer, enabling flow reattachment within an extremely short streamwise distance. Consequently, even under the high-kinetic-energy incoming flow at Ma = 0.3, the flow remains attached over a large downstream extent, effectively suppressing the dramatic increase in pressure drag caused by large-scale separation.

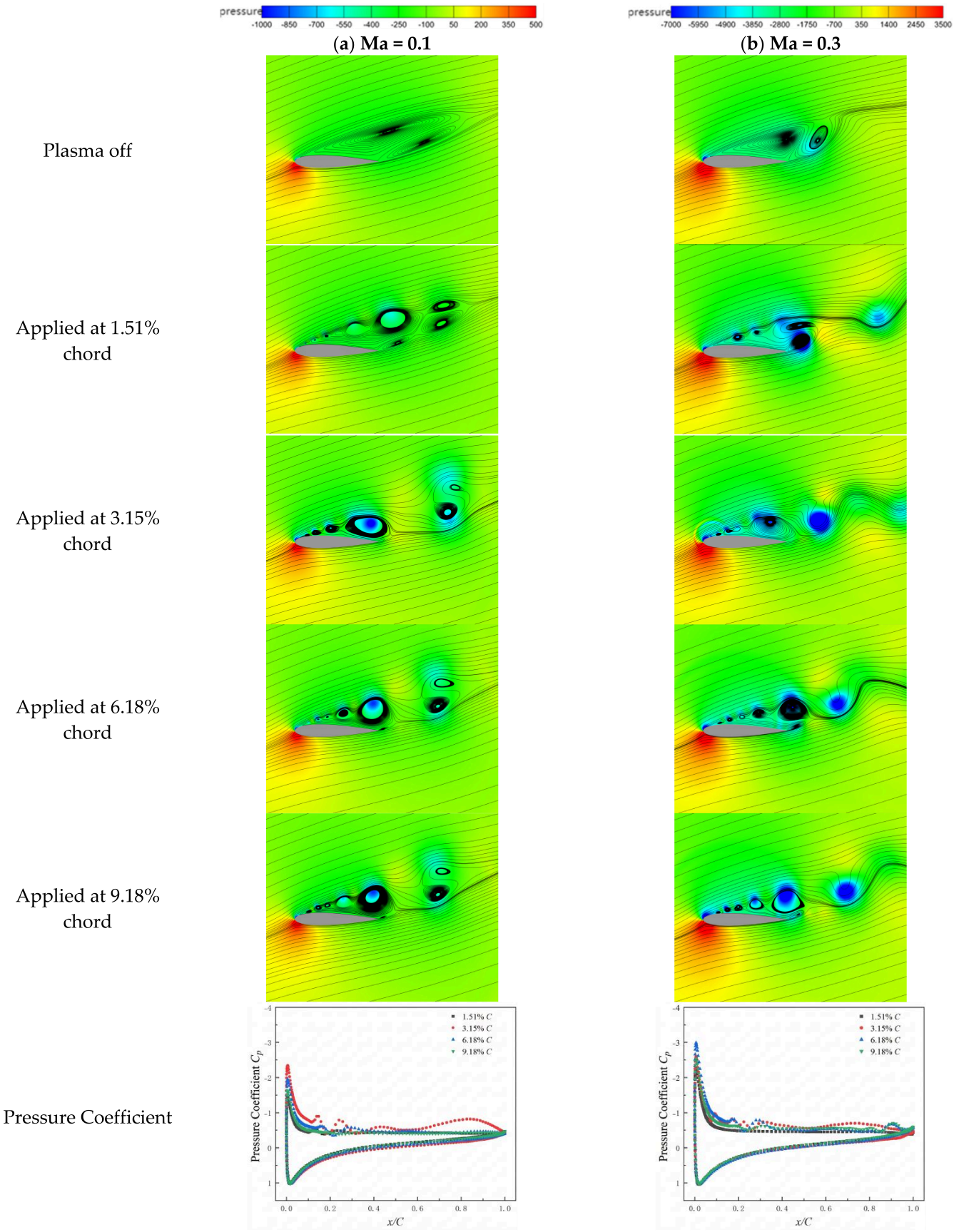


Figure 11. Plasma actuation effects at different installation positions.

At *Ma* = 0.3, the compressibility effect causes the peak suction point near the leading edge to shift downstream, and the sensitive region for laminar separation inception moves

accordingly to approximately 6.18%c compared with the Ma = 0.1 case. At this condition, the actuation location coincides exactly with the separation zone, so that all control energy is precisely deposited into the initial stage of separation—constituting suppression at the source rather than a passive remedy. Meanwhile, the local small-scale vortices induced at this position couple perfectly with the dominant instability modes of the separated shear layer at Ma = 0.3, maximizing the momentum mixing effect and enabling flow reattachment within an extremely short streamwise distance. This effectively avoids the trailing-edge secondary separation observed when the same actuation location is applied under the Ma = 0.1 condition.

Therefore, the optimal selection of the plasma actuation position is not fixed but depends on the comprehensive coupling of the free-stream Mach number and the characteristics of the leading-edge shear layer.

3.2.2. Effect of Excitation Frequency

The previous section systematically investigated the influence of plasma actuation on the aerodynamic characteristics of the pitching NACA0015 airfoil under different angles of attack and various installation positions along the leading edge. This section further focuses on the key parameter of plasma actuation frequency to explore its regulatory effect on the aerodynamic performance of the airfoil. Based on the conclusions from the previous computational analysis—whereby plasma actuation installed closer to the leading edge yields a more significant enhancement in aerodynamic characteristics—the actuation scheme with an intensity factor of κ = 1 is adopted by default for studying the influence of frequency in this section. Furthermore, the optimal actuation positions are determined for different free-stream Mach numbers: when the free-stream velocity is Ma = 0.1, the optimal actuation position is at 3.15%c chord length above the airfoil leading edge; when the free-stream velocity is Ma = 0.3, the actuator is placed at 6.18% c chord length above the airfoil leading edge. Other airfoil operating conditions remain consistent with those in the previous section. The evolution laws of the aerodynamic characteristics of the NACA0015 airfoil under different dimensionless frequencies are $F^+ = fc/v_\infty$ = 1,2,4,5 systematically studied, and the calculation results are as follows:

As can be seen from Figure 12, under the low Mach number condition of Ma = 0.1, the flow field structures exhibit significant differences at different actuation frequencies: When F^+ = 1 multiple small-scale discrete vortices form on the upper surface of the airfoil. The vortex cores are relatively dispersed, resulting in a mild momentum supplementation to the boundary layer; although the separation zone shrinks, a distinct low-pressure region remains. When F^+ = 2, the increased actuation frequency leads to a synchronous increase in the generation frequency and intensity of the vortex cores. Multiple vortex cores form a negative pressure zone in the mid-leading edge region of the airfoil, effectively blocking the upward development of the separated flow and significantly enhancing streamline reattachment. When F^+ = 4, the scale of the vortex cores further increases, and the traction effect of single large vortex cores dominates the flow field. The separation zone is compressed into small-scale discrete regions, and the momentum transport efficiency of the boundary layer reaches its peak. When F^+ = 5, excessively high actuation frequency causes the vortex structures to become overly fragmented. The energy of multiple small vortices is dispersed, weakening the continuous momentum supplementation to the boundary layer, and the separation zone shows a slight rebound trend.

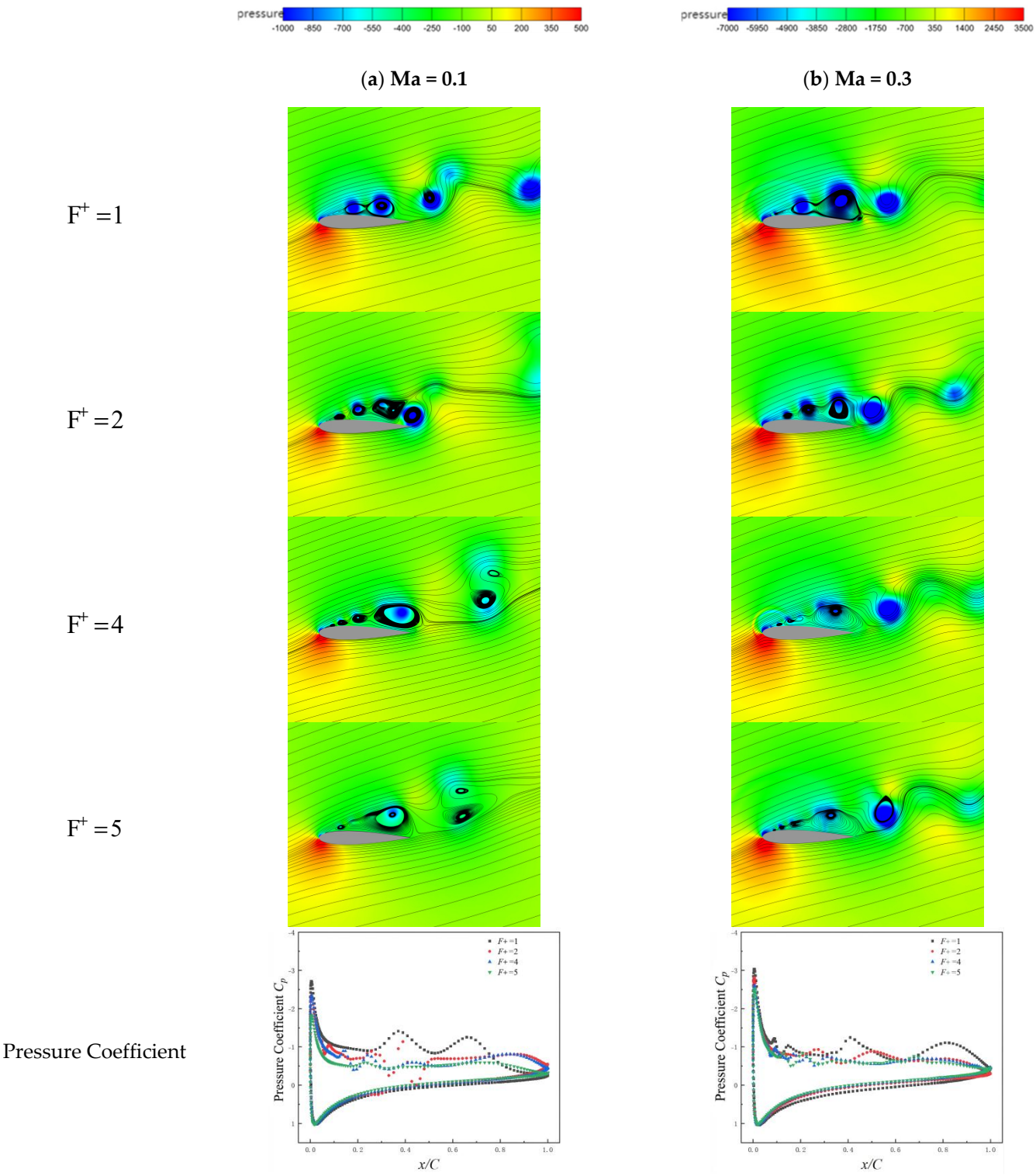


Figure 12. Flow field structure and Pressure Coefficient of the airfoil under different actuation frequencies.

Under the medium Mach number condition of Ma = 0.3, the flow field regulation characteristics with respect to actuation frequency are basically consistent. To further quantify the regulatory effects of different dimensionless frequencies (F^+ = 1,2,4,5) on the pressure field and aerodynamic characteristics of the airfoil under Ma = 0.1 and Ma = 0.3 conditions, this section analyzes the pressure coefficient (*Cp*) distribution curves, thereby deepening the understanding of the frequency mechanism from a quantitative perspective.

At $F^+ = 1$, the negative pressure peak on the upper surface of the airfoil is the highest. Meanwhile, it can be observed that under different operating conditions, higher actuation frequencies correspond to lower negative pressure peaks. This is because the mutual mixing of multiple vortices reduces their suction capability to some extent.

3.2.3. Effect of Excitation Intensity

In actual operation, helicopter rotors experience varying external flow conditions (such as velocity and turbulence intensity), which leads to changes in the energy input requirements for plasma actuation. This makes the study of actuation intensity—a key parameter—particularly necessary, as it directly determines the magnitude of momentum input into the boundary layer by the plasma actuation, thereby influencing the effectiveness of separation suppression and the final state of the flow field.

In view of this, this section focuses on the plasma control effects under different actuation intensities. By comparatively analyzing the variations in airfoil flow field structures and pressure distributions, it reveals the regulatory mechanism of actuation intensity on separation suppression. This provides a basis for matching intensity with effectiveness for the engineering application of plasma flow control on helicopter rotors, further perfecting the theoretical and methodological system of plasma active control technology in rotor aerodynamic optimization.

The static temperature distribution is a direct manifestation of plasma energy input. As shown in Figure 13, the static temperature fields exhibit significant differences under different actuation intensities. When $\kappa = 0.7$, the region of static temperature rise is small, and the temperature gradient is gentle. As the actuation intensity increases, both the extent of the static temperature rise region and the peak temperature increase, with the temperature gradient becoming steeper. When $\kappa = 1.6$, the static temperature peak reaches its maximum, and the high-temperature zone extends over the widest range along the airfoil surface.

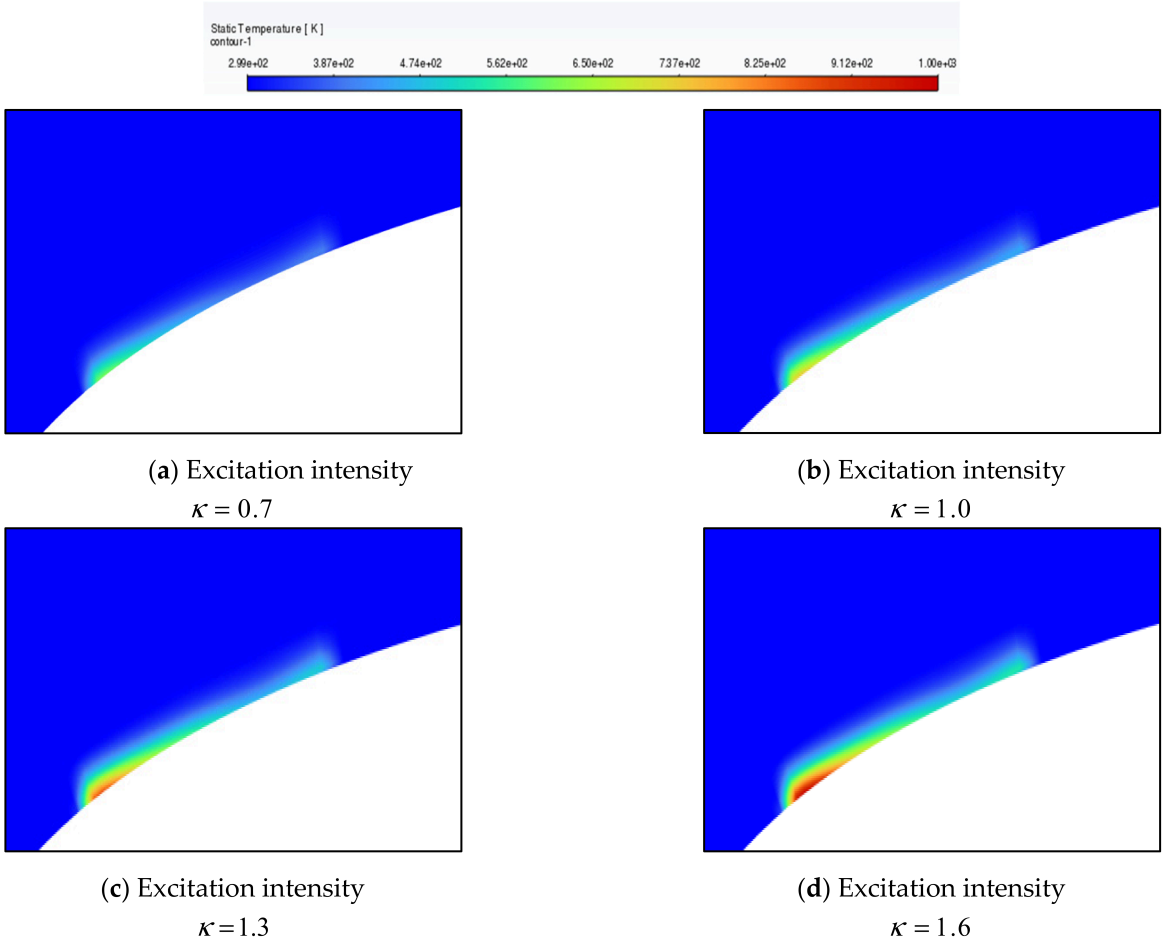
3.3. Aerodynamic Characteristics Under Plasma Control During Deep Dynamic Stall

3.3.1. Control Effectiveness of Different Plasma Actuation Modes

This section further selects an oscillating airfoil under deep stall conditions as the research object to systematically compare the regulatory effects of two plasma actuation forms—nanosecond pulse dielectric barrier discharge (NS-DBD) and alternating current dielectric barrier discharge (AC-DBD)—on the dynamic stall process of the rotor airfoil. The operating conditions considered are a mean angle of attack $\alpha_0 = 11^\circ$ and a pitching amplitude $\alpha = 9^\circ$, under which the airfoil undergoes a significant deep stall process within one azimuthal cycle.

Figure 14 presents the variation curves of aerodynamic coefficients with azimuth angle under deep stall conditions for different plasma control strategies. As shown in Figure 14a, within the azimuth angle range of 0–200°, the lift coefficient variations for the three cases are basically consistent. During this phase, the airfoil angle of attack is relatively small, and the flow remains primarily attached, resulting in limited influence of plasma actuation on aerodynamic forces. When the azimuth angle exceeds approximately 240°, the instantaneous angle of attack of the airfoil increases rapidly and surpasses the static critical stall angle. The baseline flow field curve exhibits a distinct lift peak in the 240–270° interval, followed by a rapid drop, indicating that the airfoil has entered a deep dynamic stall state accompanied by significant aerodynamic hysteresis. Compared to the baseline case, the NS-DBD controlled case shows a significantly increased lift peak during the pitch-up phase, a smoother decline after the peak, and a faster lift recovery during the pitch-down phase. This indicates that nanosecond pulse plasma can effectively weaken

the intensity of deep stall, reduce the sudden drop in lift, and alleviate hysteresis effects. Although the AC-DBD controlled case also demonstrates a certain lift enhancement effect in the deep stall region, its lift peak and overall amplitude increase are lower than those of the NS-DBD case, suggesting that alternating current plasma has relatively limited capability in regulating deep stall under these operating conditions.



(**a**) Excitation intensity $\kappa = 0.7$

(**b**) Excitation intensity $\kappa = 1.0$

(**c**) Excitation intensity $\kappa = 1.3$

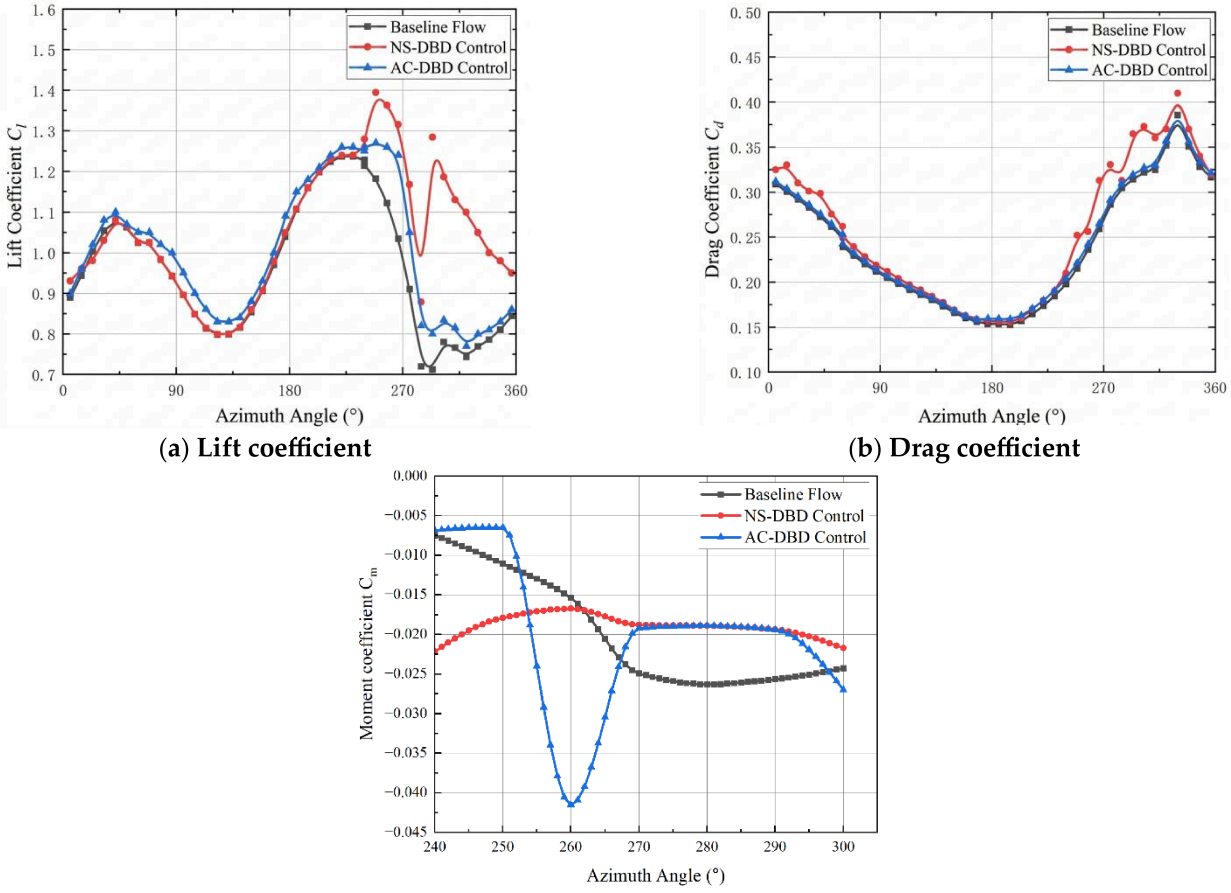
(**d**) Excitation intensity $\kappa = 1.6$

Figure 13. Temperature distribution at the leading edge of the airfoil under different actuation intensities.

The drag coefficient curves shown in Figure 14b indicate that within the azimuth angle range of 0–180°, the drag coefficients for the three cases are relatively close, primarily dominated by viscous drag under attached flow conditions. Upon entering the deep stall region of 240–300°, the drag coefficient of the baseline flow field rises significantly, corresponding to a sharp increase in pressure drag caused by large-scale leading-edge separation vortices and thick wakes. Although NS-DBD control leads to an increase in drag (due to lift-dependent drag resulting from increased lift), it effectively suppresses the surge in pressure difference drag caused by large-scale separation, thereby improving the aerodynamic efficiency of the rotor.

The moment coefficient curves shown in Figure 14c, under the baseline flow condition, the moment coefficient gradually decreases with increasing azimuth and remains at approximately -0.026 beyond 270°, indicating that the airfoil sustains a relatively strong nose-down moment. After NS-DBD control is applied, the curve becomes smoother with an overall reduction in negative moment. This reveals that the induced flow of NS-DBD can suppress flow separation and promote flow reattachment, thereby improving the pitching stability. For AC-DBD, an abrupt drop to approximately -0.042 occurs near 260°, demon-

strating that continuous alternating-current excitation may intensify local unsteady vortex structures or trigger the concentrated shedding of separation vortices, which leads to a remarkable increase in instantaneous nose-down moment.



(**a**) **Lift coefficient** (**b**) **Drag coefficient**

(**c**) **Moment coefficient**

Figure 14. Variation in aerodynamic force with azimuth angle for different plasma installation positions under deep stall condition.

3.3.2. Synergistic Effects of the Combined Control Strategy

Based on the systematic analysis in the previous section regarding the optimization effects of nanosecond pulse dielectric barrier discharge (NS-DBD) and alternating current dielectric barrier discharge (AC-DBD) on the aerodynamic characteristics of rotor airfoils under unsteady separation conditions, this section further investigates the combined application strategy of these two actuators, focusing on the evolution characteristics of unsteady separation during the dynamic stall process. Dynamic stall exhibits significant periodic azimuthal characteristics: in the 0–240° sector, the flow attachment is strong and separation development is weak; whereas in the 240–360° sector, driven by the rapid increase in the relative angle of attack and the generation and shedding of leading-edge vortices, sudden separation, main vortex formation, and lift hysteresis are particularly prominent, making it the key interval for the evolution of unsteady aerodynamic characteristics. Considering the sustained advantage of AC-DBD in regulating low-frequency unsteady shear layers, as well as the high efficiency of NS-DBD in disrupting initial leading-edge separation and breaking down large-scale vortices through strong pulse disturbances, this section constructs a combined control scheme based on azimuthal zoning: only AC-DBD is activated in the 60–220° sector to maintain continuous energy supplementation to the boundary layer; in the 220–360° and 0–60° sectors, both NS-DBD and AC-DBD are simultaneously activated at

the leading edge. This approach leverages the coupling mechanism between strong pulse regulation of vortex generation and AC actuation for maintaining steady flow, thereby synergistically suppressing the formation and shedding of large-scale leading-edge separation vortices. In this section, the parameters for the nanosecond pulse plasma actuator are set to $\kappa = 1.6$ and $F^+ = 2$, with an installation position at 3.15%c, while the AC-DBD plasma actuator is installed at 6.18%c. All other settings remain unchanged.

As shown in Figure 15, during the high-angle-of-attack pitch-up phase of deep stall (240–270°), the flow field topology of the combined actuation case (middle column) is basically consistent with that of the single NS-DBD case, both exhibiting a reduction in the scale of separation vortices and a slight refinement of the wake. Compared to NS-DBD alone, the boundary of the separation region on the upper surface in the combined control case adheres more closely to the airfoil surface, and the recirculation zone is slightly compressed. In the corresponding *Cp* scatter plots, the negative pressure at the leading-edge suction peak for the combined control case is slightly higher than that for the single NS-DBD case, while the pressure distribution in the trailing-edge region remains basically consistent, indicating very limited overall differences. This suggests that during the high-angle-of-attack pitch-up phase of deep stall, single NS-DBD actuation is already sufficient to significantly weaken large-scale leading-edge separation, and the marginal benefit of the additional momentum provided by AC-DBD is relatively small at this stage, resulting in insignificant differences in aerodynamic improvement between the two.

During the high-angle-of-attack pitch-down phase of deep stall (270–300°), the flow field characteristics of the combined actuation show more significant improvements: the large-scale separation vortices on the upper surface are further broken up, with vortex structures stretched along the chordwise direction and decomposed into multiple smaller vortex clusters. The streamlines near the wall on the upper surface exhibit clear attachment, and the wake thickness is further reduced. In the corresponding *Cp* scatter plots, the recovery amplitude of the leading-edge suction peak for the combined control case is significantly higher than that for the single NS-DBD case. Furthermore, the pressure distribution in the mid-to-aft section transitions from an approximate plateau shape to a variation with a more reasonable gradient, indicating a significant expansion of the effective attached area on the upper surface. At this stage, it can be observed that the strong pulse disturbance of NS-DBD helps to break down large-scale stall vortices, while the near-wall jet induced by AC-DBD provides continuous momentum to the boundary layer on this basis, achieving the transport and clearance of low-speed recirculation zones. The two form a synergistic "breakup–transport" effect, accelerating flow reattachment. This also explains why the combined actuation yields better results only during the pitch-down phase: under the experimental conditions of this study, the maximum induced velocity is approximately 6 m/s, which is far lower than the free-stream velocity. Therefore, its momentum injection effect is weak in attached flow or high-momentum flow regions; however, in low-speed recirculation zones or separation regions, its induced jet possesses relatively significant flow transport capability.

As shown in Figure 16, in the azimuthal angle range characterized by low angles of attack and attached flow, the *Cl* values for the three cases basically coincide, indicating that plasma actuation has a minor impact on the overall aerodynamic forces at this stage. Upon entering the deep stall region, the curve for single NS-DBD actuation is consistently higher than that of the baseline flow field, demonstrating that pulse actuation achieves significant lift preservation by weakening leading-edge separation and reducing the intensity of stall vortices. The curve for combined control is further elevated above that of single NS-DBD in the same azimuthal segment, with the lift gain relative to single NS-DBD being particularly significant during the pitch-down phase after 270°. This is highly consistent with the

flow field characteristics mentioned earlier, where the "breakup–transport" synergistic mechanism promotes rapid flow reattachment.

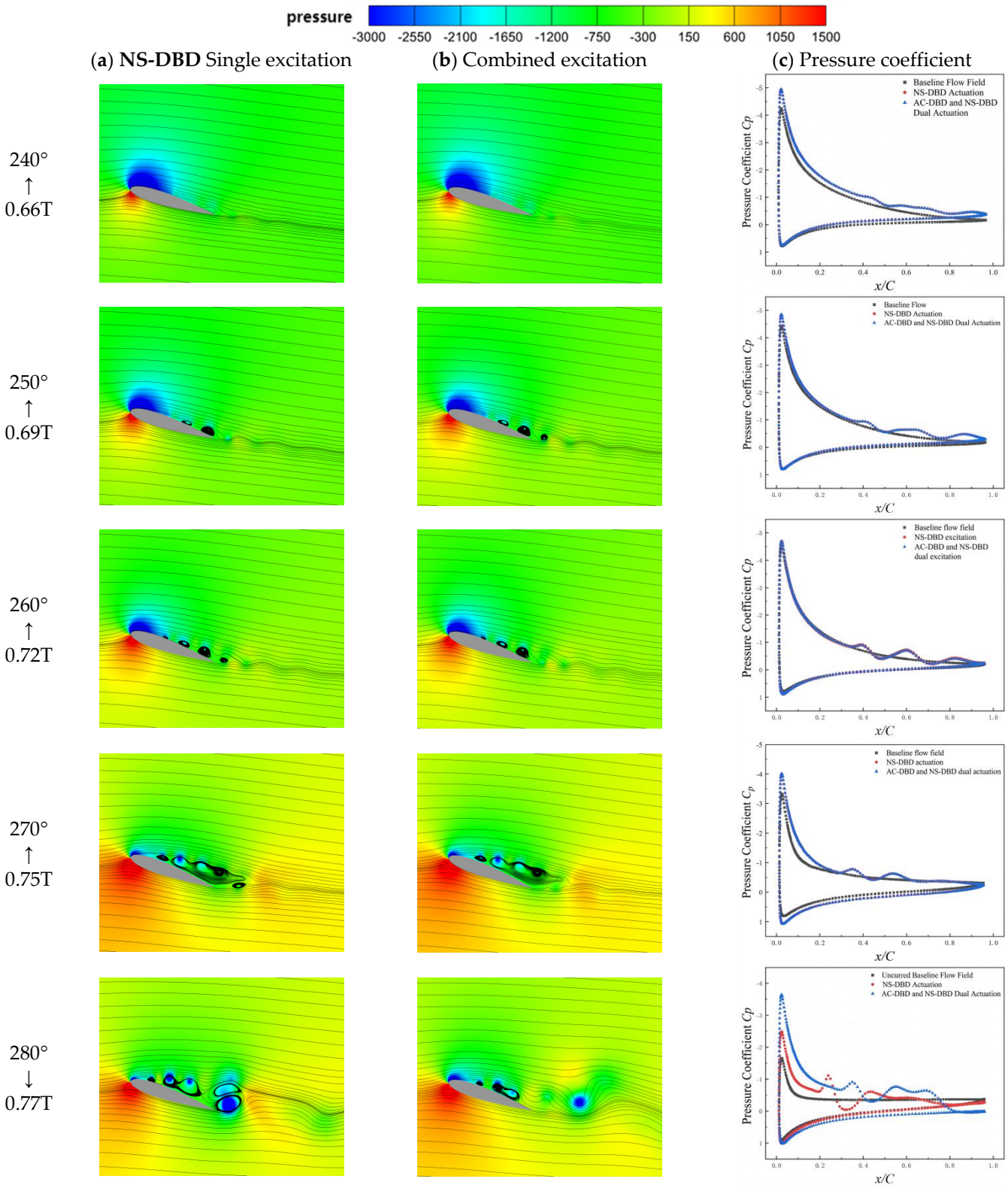


Figure 15. *Cont.*

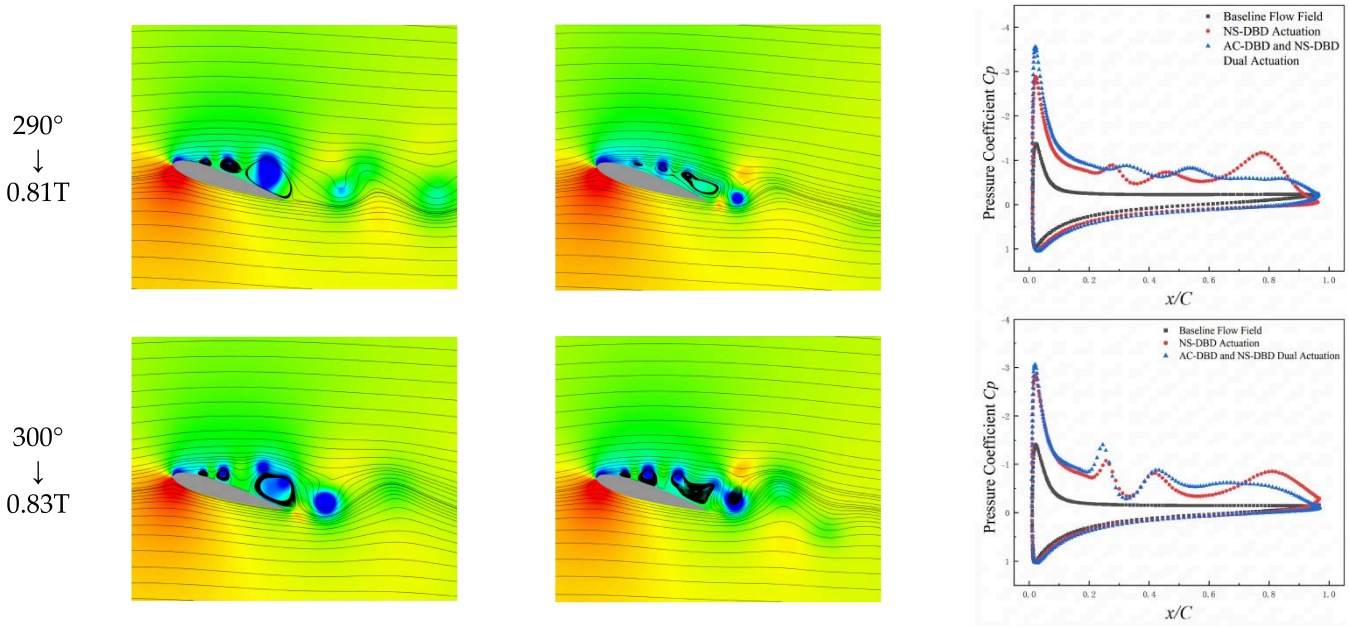


Figure 15. Control effect of combined plasma on dynamic stall vortex near 270° azimuth angle under deep stall condition (↑: pitch-up; ↓: pitch-down).

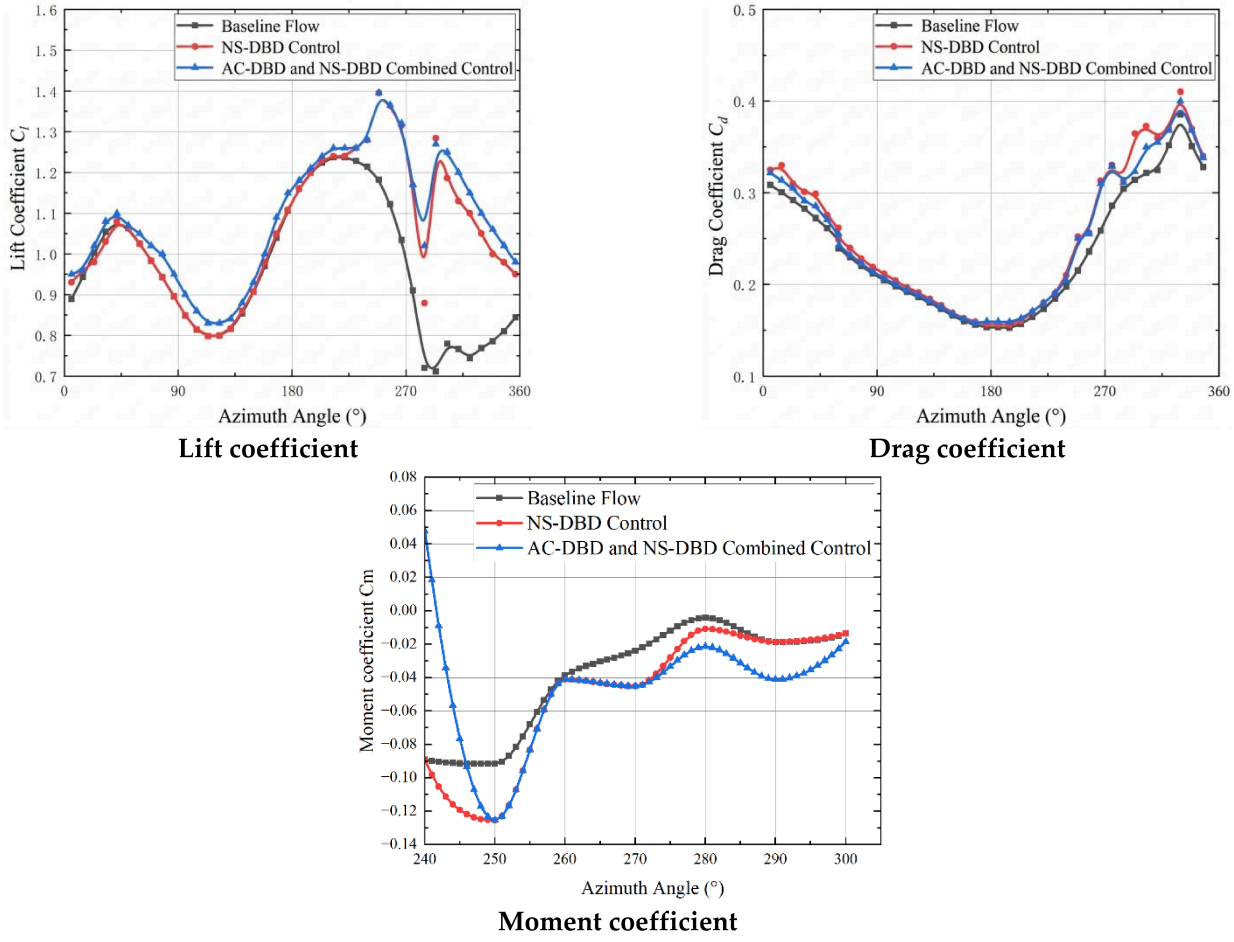


Figure 16. Variation in aerodynamic force with azimuth angle for the combined plasma installation position under deep stall condition.

The baseline flow field exhibits a distinct drag peak in the deep stall region, corresponding to a significant increase in pressure drag caused by large-scale separation vortices

and thick wakes. Although both NS-DBD actuation and combined actuation show an increase in the drag peak, this is primarily due to the substantial increase in lift-dependent drag resulting from the significant lift enhancement, as well as the high leading-edge suction component generated by maintaining attached flow at high angles of attack. Notably, combined control further suppresses the drag peak during the pitch-down phase after 270° and maintains lower *Cd* values over a wider azimuthal range. This aligns with the flow field characteristics observed under combined control, where the separation region on the upper surface is significantly shortened and the wake is markedly refined, indicating that combined control not only enhances lift but also effectively mitigates the increase in drag during the dynamic stall process.

Under the baseline condition, a relatively large negative moment of approximately −0.09 is maintained from 240° to 250°, followed by a gradual recovery. NS-DBD stabilizes the moment at roughly −0.02 in the later stage, significantly attenuating the nose-down moment. The combined control can rapidly raise the moment in the initial phase and shorten the duration of high negative moment, indicating that AC excitation enhances the momentum supply of the flow. Nevertheless, large negative moment is observed near 250° and after 285° for the combined control scheme. Its advantages are mainly reflected in the transient recovery rate.

4. Discussion

This study systematically compares the performance differences between AC-DBD and NS-DBD plasma actuators for dynamic stall control on the retreating side of rotor blades at high advance ratios through numerical simulations. The results demonstrate that the two actuator types exhibit distinctly different control characteristics at different stages of the dynamic stall cycle, a disparity rooted in their fundamentally different physical mechanisms.

The AC-DBD actuator continuously injects momentum into the boundary layer through the "ionic wind" effect, enhancing the streamwise momentum of near-wall fluid and thereby improving the boundary layer's ability to resist the adverse pressure gradient and delaying separation onset. During the upstroke phase of the present study, the continuous momentum injection from AC-DBD significantly postpones the separation onset angle of attack, allowing the boundary layer to remain attached at higher angles of attack. However, under high-Reynolds-number conditions, the momentum-injection intensity of AC-DBD is relatively limited compared to the freestream momentum, and its control effectiveness decays rapidly with increasing freestream velocity. This explains why AC-DBD alone exhibits insufficient suppression capability for deep dynamic stall vortices under the high-freestream-velocity conditions of high-advance-ratio rotors. In contrast, the NS-DBD actuator generates localized rapid heating and compression waves (micro-shock waves) through nanosecond high-voltage pulses, interacting with the separated shear layer via thermal perturbations. The pulsed thermal perturbations of NS-DBD can excite natural instabilities within the shear layer, promoting the formation of large-scale coherent structures that "bleed off" leading-edge vorticity and attenuate the dynamic stall vortex intensity. In the present study, NS-DBD demonstrates superior control capability during the stall-development and downstroke phases, effectively reducing aerodynamic hysteresis and accelerating flow reattachment. However, the control effectiveness of NS-DBD during the upstroke phase is extremely limited, because the shear-layer instability has not yet fully developed at this stage, and the pulsed thermal perturbations lack an unstable mode to be amplified. The above comparison clearly indicates that AC-DBD and NS-DBD possess inherent complementarity in dynamic stall control: AC-DBD excels at "prevention"—delaying onset through momentum injection before separation occurs; NS-

DBD excels at "remediation"—weakening the vortex structure and promoting reattachment through thermal perturbations after separation has occurred. Owing to the singularity of their physical mechanisms, a single actuator type cannot provide full-cycle effective control throughout the entire dynamic stall process.

Actuation frequency is a key parameter affecting the effectiveness of plasma-based dynamic stall control. The observed differences in control effectiveness at different frequencies can be explained from the perspective of the timescale competition between the two thermal perturbations of NS-DBD—compression waves and residual heat. When the dimensionless actuation frequency is low (e.g., $F^+ = 1$), the time interval between successive pulses is relatively long, allowing the residual heat to dissipate fully before the next pulse arrives, and each actuation event acts on the flow field primarily as an independent compression-wave event. At this frequency, the actuation frequency forms a "frequency-locking" effect with the natural shedding frequency of the dynamic stall vortex, enabling the most effective coupling with the leading-edge vortex structure and thus producing the highest leading-edge suction peak. Existing experimental studies have also shown that the optimal performance of unsteady plasma control occurs in the $F^+ = 1\sim2$ range. When the actuation frequency is high (e.g., $F^+ = 4$), the pulse interval shortens and the cumulative effect of residual heat intensifies significantly, forming a sustained localized heating zone within the boundary layer. This sustained thermal perturbation alters the effective viscosity and velocity profile of the near-wall fluid, thereby more effectively suppressing the onset of separation. Therefore, $F^+ = 4$ performs best in terms of the specific metric of "delaying stall onset." $F^+ = 2.0$ lies in the transition regime between the two mechanisms. At this frequency, it retains a certain degree of residual-heat accumulation to maintain a sustained influence on the boundary layer while also achieving a certain level of coupling with the vortex shedding frequency. Consequently, $F^+ = 2.0$ represents a compromise in overall performance—although not optimal in any single metric, it achieves the best balance in comprehensive control benefits (lift enhancement and hysteresis reduction).

The core novelty of the azimuthal-zone plasma combined control strategy proposed in this study lies in the differentiated application of AC-DBD and NS-DBD at different azimuthal angles (corresponding to different phases) according to the phase-dependent characteristics of dynamic stall evolution, thereby achieving temporal complementarity between the two actuator types. The dynamic stall process can be divided into four typical phases: the upstroke phase, stall-onset phase, vortex-shedding phase, and reattachment phase. Different phases exhibit different flow characteristics and control requirements. During the upstroke phase, the boundary layer gradually thickens and the adverse pressure gradient intensifies; the primary control requirement at this stage is to delay separation onset. AC-DBD's continuous momentum injection plays the dominant role at this stage—injecting momentum into the boundary layer through the ionic-wind effect and enhancing the boundary layer's ability to resist the adverse pressure gradient. NS-DBD is nearly ineffective at this stage because the shear-layer instability has not yet fully developed and the pulsed thermal perturbations lack an unstable mode to be amplified. The combined case behaves similarly to AC-DBD alone at this stage, which precisely validates the rationality of the phase-distribution strategy—AC-DBD compensates during the phase where NS-DBD is "ineffective." During the stall-development phase, the separated shear layer has formed and the dynamic stall vortex begins to roll up. At this point, NS-DBD's pulsed thermal perturbations can effectively couple with the unstable modes of the shear layer, "bleeding off" leading-edge vorticity and attenuating the dynamic stall vortex intensity by exciting large-scale coherent structures. Meanwhile, the momentum pre-injected by AC-DBD has already altered the local velocity profile, making the boundary-layer velocity distribution fuller, which provides a more favorable background flow field for the NS-DBD-induced

vortex structures, endowing them with higher strength and longer survival time. The combined case significantly outperforms either individual actuation at this stage, demonstrating true "1 + 1>2" enhancement. During the downstroke and reattachment phase, NS-DBD alone already significantly increases the lift coefficient and reduces aerodynamic hysteresis. AC-DBD's continuous actuation at this stage further maintains boundary-layer momentum and accelerates the flow reattachment process. Through the superposition of AC-DBD's continuous action and NS-DBD's pulsed action, the combined case achieves earlier reattachment and smaller aerodynamic hysteresis. The core physical mechanism of synergistic enhancement revealed in this study can be summarized as follows: AC-DBD's continuous momentum injection provides a "more favorable background flow field" for NS-DBD's pulsed thermal perturbations—a fuller boundary-layer velocity profile and stronger tolerance to the adverse pressure gradient—making compression-wave-induced perturbations more easily amplified and rendering the modulating effect of residual heat more persistent. By modifying the momentum distribution and stability characteristics of the local flow field, the two actuators together achieve comprehensive control effectiveness that cannot be attained by a single actuation mode. Quantitative analysis shows that the synergistic control achieves a 13.8% increase in lift and a 20% reduction in lift-coefficient hysteresis-loop area, with control benefits significantly superior to those of single-actuation modes. Existing experimental studies have shown that unsteady plasma actuation can reduce the lift hysteresis-loop area by more than 16% and increase the mean lift coefficient by 6%; under specific conditions, unsteady actuation can reduce the lift hysteresis-loop area by more than 30%. The predicted results of the present study fall within the reasonable range of the above experimental data, further supporting the effectiveness of the synergistic strategy.

It should be noted that the present study is a proof-of-concept numerical investigation, and the effectiveness of the proposed combined control strategy ultimately requires experimental verification. Research institutions have already accumulated substantial experience in wind-tunnel experiments on plasma-based dynamic stall control, and subsequent work will continue to advance in this direction. In addition, the present study focuses primarily on lift and drag characteristics, without a detailed discussion of pitching moment. The pitching-moment excursions induced by dynamic stall are a critical factor affecting rotor structural safety and flight quality. Future work will establish a comprehensive evaluation framework encompassing pitching moment and aerodynamic damping to more thoroughly assess the engineering value of the combined control strategy.

Author Contributions: W.K.: Conceptualization, Methodology, Formal analysis, Writing—original draft, Writing—review and editing, Supervision.; T.W.: Software, Validation, Investigation, Data curation, Visualization, Writing—original draft.; P.Z.: Methodology, Resources, Writing—review and editing, Project administration. All authors have read and agreed to the published version of the manuscript.

Funding: This research received no external funding.

Data Availability Statement: The datasets generated and/or analyzed during the current study are available from the corresponding author upon reasonable request.

Conflicts of Interest: The authors declare that there are no conflicts of interest regarding the publication of this paper. The research was conducted in the absence of any commercial or financial relationships that could be construed as potential conflicts of interest.

Nomenclature

ρ	Air density	u	x-component of velocity
v	y-component of velocity	μ	Fluid dynamic viscosity
c	Airfoil chord length	μ_∞	Freestream dynamic viscosity
p	Fluid pressure	E	Electric field intensity
E_x, E_y	Spatial distribution of electric field strength in the x- and y-directions	k_1	Electric field gradient constant in the x-direction
k_2	Electric field gradient constant in the y-direction	x, y	Spatial coordinates of plasma distribution
U	Discharge voltage	k	Reduced frequency
d	Gap distance	E_0	Maximum electric field intensity
α	Airfoil angle of attack	f_x, f_y	Spatial distribution of Lorentz force in the x- and y-directions
R	Rotor radius	f	Discharge frequency
E_{cr}	Breakdown electric field strength	t	Physical time
ϑ	Excitation frequency	N	Gas number density
$F_{tave,x}$	Time-averaged volumetric force in the x-direction	$F_{tave,y}$	Time-averaged volumetric force in the y-direction
ρ_c	Charge density	e_c	Elementary charge
C_l	Lift coefficient	C_d	Drag coefficient
C_P	Pressure coefficient	η	Fraction of energy transferred into fast gas heating
S	Two-dimensional volumetric force source term in vector form	M_a	Mach number
κ	Intensity control parameter for NS-DBD	$\Re$	Intensity control parameter for AC-DBD
T_s	Sutherland temperature	Δt	Discharge time
T	Freestream temperature	U_∞	Freestream velocity
a_0	Mean angle of attack	a_1	Amplitude of the angle of attack
F^+	Dimensionless excitation frequency	Re	Reynolds number
T	Fluid temperature	δ_{ij}	Kronecker delta function
λ	Heat transfer coefficient		

References

1. Carr, L.W. Progress in analysis and prediction of dynamic stall. *J. Aircr.* **1988**, *25*, 6–17. [CrossRef]
2. Greenblatt, D. Active control of dynamic stall: A review. *Prog. Aerosp. Sci.* **2026**, *164*, 101221. [CrossRef]
3. McCroskey, W.J. *The Phenomenon of Dynamic Stall*; NASA TM-81264; NASA Ames Research Center Moffett Field: Mountain View, CA, USA, 1981.
4. Li, G.Q.; Zhao, X.H.; Yi, S.H.; Song, K.; Zhao, G. Research progress on rotor reverse flow and dynamic stall flow control methods. *J. Exp. Fluid Mech.* **2023**, *37*, 29–47.
5. Doosttalab, M.; Ferreira, C.S.; Ragni, D.; Yu, W.; Rautmann, C. Vortex Generator Effects on Dynamic Stall of Thick Airfoils. *Renew. Energy* **2025**, *255*, 123746. [CrossRef]
6. Greenblatt, D.; Wygnanski, I.J. The Control of Flow Separation by Periodic Excitation. *Prog. Aerosp. Sci.* **2000**, *36*, 487–545. [CrossRef]
7. Han, Z.H.; Song, W.P.; Qiao, Z.D. Numerical Simulation of Active Dynamic Stall Control on an OA212 Rotor Airfoil. *Acta Aerodyn. Sin.* **2009**, *27*, 639–644.
8. Wilkie, W.K.; Wilbur, M.L.; Mirick, P.H.; Cesnik, C.E.S.; Shin, S.J. Aeroelastic Analysis of the NASA/Army/MIT Active Twist Rotor. In Proceedings of the American Helicopter Society 55th Annual Forum, Montreal, QC, Canada, 25–27 May 1999.
9. Nozari, M.; Ebrahimi, A. Closed-Loop Control of Dynamic Stall on a Pitching Airfoil with Tandem Configuration of Plasma Actuators. *Phys. Fluids* **2025**, *37*, 087170. [CrossRef]
10. Yu, H.; Zheng, J. Numerical investigation of control of dynamic stall over a NACA0015 airfoil using dielectric barrier discharge plasma actuators. *Phys. Fluids* **2020**, *32*, 035103. [CrossRef]
11. Yang, H.; Liang, H.; Zhao, G.; Wang, B.; Zhang, S.; Kong, W. Experimental study on dynamic stall control based on AC-DBD actuation. *Plasma Sci. Technol.* **2021**, *23*, 115502. [CrossRef]
12. Li, G.; Chang, Z.; Zhang, X.; Ma, Z.; Wang, C.; Yi, S. Experimental Investigation of Dynamic Stall Control on a Rotor Airfoil Using Unsteady Dielectric Barrier Discharge. *Acta Aerodyn. Sin.* **2024**, *42*, 64–71.

13. Zhang, H.; Yu, H.; Zhang, A.; Zheng, J. Large eddy simulation of dynamic stall over an airfoil and its control with plasma actuator. *AIP Adv.* **2023**, *13*, 025218. [CrossRef]
14. Takashima, K.; Kimura, T.; Yamasaki, H. Experimental Study on DBD Plasma Actuator with Combination of AC and Nanosecond Pulse Voltage. *Electr. Eng. Jpn.* **2013**, *185*, 21–29. [CrossRef]
15. Long, Y.; Li, H.; Meng, X. Flow Control Over a Slender Forebody Using AC and NS-DBD Plasma Actuators. *Adv. Aeronaut. Sci. Eng.* **2014**, *5*, 358–363.
16. Zhao, G.Y.; Yang, Y.D.; Li, T.T.; Xiao, C.H.; Yan, L. Vorticity transport characteristics of separated shear layer under AC/NS-DBD plasma actuation. *Acta Aerodyn. Sin.* **2023**, *41*, 48–60.
17. Yu, H.; Zheng, J. Investigation of Flow Separation and Its Control Over Rotor Blades in Forward Flight with Plasma Actuator. *Int. J. Heat Mass Transf.* **2025**, *245*, 127023. [CrossRef]
18. Sato, M.; Nonomura, T.; Okada, K. Experimental and numerical investigations of flow control by a dual-mode plasma actuator. *AIAA J.* **2019**, *57*, 3215–3227.
19. Zhao, G.Y.; Li, Y.H.; Liang, H.; Hua, W.Z.; Han, M.H. Phenomenological simulation of nanosecond pulse surface dielectric barrier plasma actuation. *Acta Physica Sin.* **2015**, *64*, 015101. [CrossRef]
20. Takashima, K.; Zuzeek, Y.; Lempert, W.R. Characterization of surface dielectric barrier discharge plasma sustained by repetitive nanosecond pulses. In Proceedings of the Adamovich I V 2010 41st Plasmadynamics and Lasers Conference, Chicago, IL, USA, 28 June–1 July 2010.
21. Shyy, W.; Jayaraman, B.; Andersson, A. Modeling of glow discharge-induced fluid dynamics. *J. Appl. Phys.* **2002**, *92*, 6434–6443. [CrossRef]
22. Singhal, A.; Castañeda, D.; Webb, N.; Samimy, M. Control of dynamic stall over a NACA 0015 airfoil using plasma actuators. *AIAA J.* **2018**, *56*, 78–89. [CrossRef]
23. Starikovskii, A.Y.; Roupassov, D.V.; Nikipelov, A.A.; Nudnova, M. *Acoustic Noise and Flow Separation Control by Plasma Actuator*; AIAA-2009-0695; AIAA: Reston, VA, USA, 2009.
24. Marco, D.; Li, J.M. Experimental study of a DBD-plasma driven channel flow. In *49th AIAA Aerospace Sciences Meeting*; AIAA: Reston, VA, USA, 2011; p. 954.

Disclaimer/Publisher's Note: The statements, opinions and data contained in all publications are solely those of the individual author(s) and contributor(s) and not of MDPI and/or the editor(s). MDPI and/or the editor(s) disclaim responsibility for any injury to people or property resulting from any ideas, methods, instructions or products referred to in the content.